J. Fluid Mech. (2024), *vol*. 978, A29, doi:10.1017/jfm.2023.984

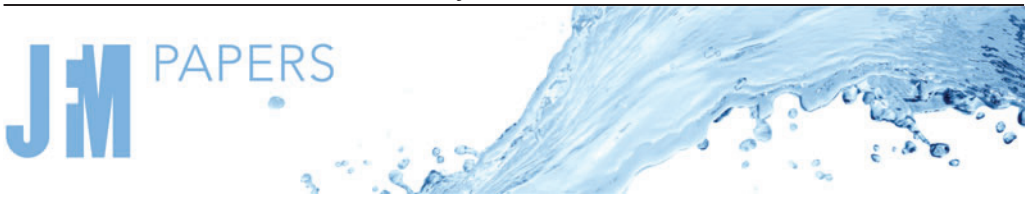

Scaling law of the second-order structure function over the entire sandstorm process

Hongyou Liu[1], **Yanxiong Shi**[1] **and Xiaojing Zheng**[2],†

[1]Center for Particle-laden Turbulence, Lanzhou University, Lanzhou 730000, PR China

[2]Research Center for Applied Mechanics, Xidian University, Xi'an 710071, PR China

(Received 5 April 2023; revised 15 November 2023; accepted 15 November 2023)

This study reveals the competitive evolutionary process of the main driving factors in the early, middle and late stages of sandstorms, as shear turbulence becomes dominant and is then suppressed by enhanced thermal stability, based on quadrant analysis of the sand-laden turbulent wind field acquired from field observations over the entire sandstorm process. Moreover, the self-organized state of multiscale structures in the energy-containing region of the sand-laden turbulence is found to change significantly as the sandstorm develops. The logarithmic scaling law that governs the cumulative turbulent kinetic energy for the non-stationary flow in the early and late stages of the sandstorm is different from the existing theoretical formula. The corresponding rate of increase in the cumulative kinetic energy with increasing scale is much higher in these stages than in the middle stage of the sandstorm with steady flow. The change in self-organized state of turbulence is responsible for the flow acceleration and the thermal superimposed effect, rather than the addition of sand particles.

Key words: atmospheric flows, particle/fluid flow, turbulent boundary layers

1. Introduction

Sandstorms, a severe disastrous weather phenomenon of broad concern (Thomas, Knight & Wiggs 2005; Fenton, Geissler & Haberle 2007; Kok 2010; An, Sin & DuBow 2015; Li *et al.* 2021), occur frequently in northern China every spring (Xu *et al.* 2020). There are at least two different plausible explanations for the causes of sandstorms from the meteorology and hydrodynamics fields. The former models the origin as thermal (buoyancy-driven) turbulence with a high Rayleigh number, which arises when a hot sandy surface encounters a cold front derived from atmospheric circulation (Dai, Williams & Qiu 2021; Helfer & Nuijens 2021). The latter models the origin as shear-driven turbulence with a friction Reynolds number ($Re_\tau = u_\tau \delta/\nu$, where δ, u_τ and ν denote the boundary layer

† Email address for correspondence: xjzheng@lzu.edu.cn

thickness, friction velocity and kinematic viscosity, respectively) as high as $O(10^6)$, which exhibits strong shearing effects on sandy surfaces and causes large amounts of sand to leave the surface (Smits, McKeon & Marusic 2011; Zhao *et al.* 2020). Previous studies on the dynamic factor of sandstorms have mainly focused on the statistical analysis of turbulence data with steady wind without gusting or sharp changes in the mean flow (Ackerman & Cox 1989; Cassisa *et al.* 2010; Cheng, Zeng & Hu 2011). The general understanding is that the shear turbulence plays a more crucial role than thermal turbulence in sand emission and transport (Zhang *et al.* 2008; Li & Zhang 2012; Zhao *et al.* 2020). However, much less is known about whether this understanding is applicable to the entire sandstorm process, especially to the early and late stages of sandstorms. The early and late stages, regarded as non-stationary flows (Chunchuzov 1994; Kareem *et al.* 2019), are the rising stage with a continuously accelerating atmospheric incoming flow and the declining stage with a decelerating flow, respectively.

The discovery of a series of coherent structures that are in some way organized in random and disordered turbulence (Robinson 1991; Jiménez 2018) was a milestone in related studies in the 1950s. Subsequently, coherent structures, even very-large-scale motions (VLSMs) with streamwise lengths $L_x > 3\delta$, were found to exist in near-neutrally stratified atmospheric surface-layer (ASL) flows, which are similar to those in the turbulent boundary layer (TBL) observed in laboratory testing with pipes (Guala, Hommema & Adrian 2006; Bailey & Smits 2010; Baltzer, Adrian & Wu 2013) and channels (Christensen & Adrian 2001; Balakumar & Adrian 2007). The VLSMs have also been found in the steady stage of sandstorms, where the wind velocity reaches a plateau after an acceleration process in the rising stage (Liu & Zheng 2021). These flows are all dominated by shear-driven turbulence (Smits *et al.* 2011; Jiménez 2018; Marusic & Monty 2019). For thermal turbulence, coherent structures with dimensions of the order of the experimental device (Sun, Xi & Xia 2005; Chong *et al.* 2015), commonly termed thermal plumes, have also been found in Rayleigh–Bénard convection (Zhou, Sun & Xia 2007; Huang *et al.* 2013; Xie, Ding & Xia 2018). In most cases, shear and thermal turbulence coexist in ASL flows, which is known as convective ASL flow (Rao & Narasimha 2006; Nguyen *et al.* 2013; Ding *et al.* 2018; Salesky & Anderson 2018; Tong & Ding 2020). According to the Monin–Obukhov similarity theory, when the potential temperature gradient is negative (i.e. the near-surface temperature is higher than that in the upper layers), the airflow moves upward and the ASL is unstably stratified (Obukhov 1946; Monin & Obukhov 1954). This upward motion of the flow under buoyancy causes the coherent structures to be lifted up from the ground, especially the heads of hairpin vortices (these are aligned coherently in the streamwise direction, creating larger-scale coherent structures, Adrian, Meinhart & Tomkins 2000), resulting in the structures becoming steeper and having a larger inclination with increasing thermal instability (Hommema & Adrian 2003; Carper & Porté-Agel 2004; Chauhan *et al.* 2013; Liu, Bo & Liang 2017; Salesky & Anderson 2018; Li *et al.* 2022). In the stable regime (positive potential temperature gradient), the sinking cold and denser air exhibits a 'suppressing' effect, resulting in a decrease in the structure inclination angle (Chauhan *et al.* 2013; Liu *et al.* 2017). The variation in the spatial length scales of coherent structures with thermal stability has a similar trend to that of the structure inclination; that is, the spatial extent is significantly increased in the unstable regime but reduced in the stable condition (Chauhan *et al.* 2010). Recently, Li *et al.* (2022) investigated the effect of thermal stability on the aspect ratio (streamwise/wall-normal scales) of self-similar coherent structures using ASL data and found that the aspect ratio becomes progressively smaller as thermal instability increases. In addition to the topology of turbulent coherent structures, thermal stability also leads to significant changes in other

flow properties, including the mean velocity profile (Salesky, Katul & Chamecki 2013; Tong & Ding 2020; Heisel *et al.* 2023), the turbulent kinetic energy (TKE) budget and the partitioning of the TKE between its streamwise, spanwise and vertical components (u^2, v^2, w^2) (Wyngaard & Coté 1971; Frenzen & Vogel 1992; Nilsson *et al.* 2019; Zou *et al.* 2020), and the velocity spectra (Kaimal *et al.* 1972; Yadav, Raman & Sharan 1996; Ding *et al.* 2018).

The second-order structure function quantitatively depicts the self-organized state of multiscale turbulent structures (She & Leveque 1994; Frisch & Kolmogorov 1995). In Rayleigh–Bénard convection, the cumulative TKE of all structures with streamwise length $L_x \leq r$, that is, the second-order structure function $S_2(r/z)$ (where z denotes the wall-normal distance), follows the power law of $(r/z)^{2/3}$ (Kolmogorov's two-thirds law) (Frisch & Kolmogorov 1995). However, in the shear turbulence, the expression has not only the two-thirds law corresponding to the inertial region of $\eta \ll r < z$ (where η denotes the Kolmogorov microscale), but also a logarithmic scaling law $\sim B\ln(r/z)$ (where B is the log–linear slope) in the energy-containing region of $z < r \ll \delta$ (Perry & Chong 1982). While the scaling for Rayleigh–Bénard convection and wall-bounded shear turbulence has been studied by experiments and numerical simulations, less attention has been paid to scaling in convective boundary layers. Then, in the evolution of sandstorms with both shear turbulence and thermal turbulence, does the second-order structure function in the sand-laden atmospheric turbulence field tend to the scaling law of thermal or shear turbulence? Does this function also evolve with sandstorm development? What are the factors leading to the evolution of the scaling law? We address these aspects in the present work.

Based on field observations of the entire sandstorm process, including the rising, steady and declining stages, this study acquires the turbulent fluctuations by removing the time-varying mean flow from the stationary and non-stationary components of the velocity time series, and then adaptive segmented processing is used to ensure ergodicity. By applying statistical analysis, it is found that the thermal turbulence and the shear turbulence exhibit a competitive evolutionary process with sandstorm development, which leads to a change in the scaling law of the cumulative kinetic energy in the sand-laden atmospheric turbulence. Specifically, during the evolution of the sandstorm, the dominant driving factor transitions from thermal turbulence to shear turbulence, which then attenuates under thermal (gravity) suppression. The structure function follows the logarithmic scaling law, but the scaling parameter gradually decreases from a large value to approach the theoretical result and finally increases slightly again, where the key factors are the accelerated flow and thermal stability of the sandstorm flow rather than the sand particles.

This work is organized as follows: the experimental set-up for the field observations in the particle-laden ASL is described in § 2. Section 3 presents the processing procedure of the sandstorm non-stationary data. After applying the data processing procedure, the flow and particle parameters are provided. The analysis of the evolution of the turbulence driving factors during the entire sandstorm process considering the Monin–Obukhov thermal stability parameter and quadrant distribution is provided in § 4. The difference in the scaling law of the second-order structure function in rising, steady and declining stages of the sandstorm and the individual effects of environmental factors on the scaling law are presented in § 5. The concluding remarks are drawn in § 6. Details of the non-stationary data processing method and a comparison of the results obtained with the non-stationary method and stationary method are provided in Appendix A. Appendix B provides results from another sandstorm data.

2. Acquisition of observational data

The data employed in the present work were derived from observation of a sandstorm starting at 16:00 local time on 14 April 2016 and ending at 06:00 on 15 April 2016 in Northwest China. In addition, to draw general conclusions, more datasets from long-term observations were selected where only one of the parameters are different and the others are similar. The field observations were conducted at an ASL turbulence observatory called the Qingtu Lake observation array (QLOA, detailed in Wang & Zheng 2016; Liu & Zheng 2021), which is located in the flat dry bed of the Qingtu Lake and borders the two deserts of Badain Jaran and Tengger in western China (E: 103°40′03″, N: 39°12′27″). This area has a flat sandy surface and is perennially dry and rainless, with no vegetation covering the ground. The QLOA is composed of a 32 m high main tower and 23 lower towers that are 5 m in height, which are arranged in similar orientations according to Cartesian coordinates. There are 11 towers along the northwest direction (prevailing wind direction, x-axis) and 6 spanwise towers (y-axis) on the left and right sides of the main tower (z-axis). Thus, the QLOA can perform synchronous multipoint measurements of the wind velocity, temperature and sand concentration in a spatial domain of 390 m, 60 m and 32 m in the streamwise, spanwise and vertical directions and is regarded as one of the two notable field stations for the study of TBLs at the atmospheric scale by Heisel *et al.* (2018). The three components of wind velocities and the temperature were measured using sonic anemometers (CSAT3B, Campbell Scientific) at a sampling frequency of 50 Hz. The PM10 (particles with diameters $\leq 10\,\mu$m) concentration was measured by an aerosol monitor (DUSTTRACK II-8530-EP, TSI Incorporated) with a sampling frequency of 1 Hz. The multi-physical quantity data used in this study were acquired at eleven heights spaced logarithmically from 0.9 m to 30 m ($z = 0.9$, 1.71, 2.5, 3.49, 5, 7.15, 8.5, 10.24, 14.65, 20.96 and 30 m). Details of the measurements of the wind velocity and the sand concentration in wind-blown sand flows/sandstorms can be found in Liu, Shi & Zheng (2022).

After applying wind direction correction to the raw flow field data (Wilczak, Oncley & Stage 2001), the actual streamwise, spanwise and vertical velocity time series (U, V, W) were acquired and are shown in figure 1(a–c). Figure 1(a) shows that the streamwise velocity of the sandstorm undergoes an initial rapid increase to a plateau and then a rapid decrease. Thus, the sandstorm can be divided into rising, steady and declining stages with durations of approximately 3, 5 and 6 h, respectively. To check the stationarity, the non-stationary index IST of streamwise velocity signals $U(t) = \{u_1, u_2, \ldots, u_N\} = \{U_1(\Delta t), U_2(\Delta t), \ldots, U_n(\Delta t)\}$ is calculated as (Foken *et al.* 2004)

$$IST = |(CV_m - CV)\,/CV| \times 100\,\%, \tag{2.1}$$

where $CV_m = (\sum_{i=1}^{n} CV_i)/n$ is the mean of CV_i, CV_i is the local variance of each segment $U_i(\Delta t)$, and CV is the overall variance of $U(t)$. For example, for hourly streamwise velocity time series, $\Delta t = 5$ min, $n = 12$ and CV is the overall variance for 1 h (standard practice in the analysis of ASL data, Wyngaard 1992). The IST measures data non-stationarity by comparing the overall variance (CV) and the average local variance (CV_m) of the selected signal, which expresses the 'relative size of the error' of the local variance in relation to global variance. The resulting hourly IST in the entire sandstorm process is shown by a blue line in figure 1(a). According to the stationary data condition of $IST < 30\,\%$ proposed in Foken *et al.* (2004), it is determined that the velocity signal of the sandstorm is wide-sense stationary (Koralov & Sinai 2007) in the steady stage, but non-stationary in both the rising and the declining stages. In addition, the synchronously measured time series of PM10 dust concentration and temperature at the corresponding height are plotted in figure 1(d,e), where the green line in figure 1(e) is the Monin–Obukhov thermal stability

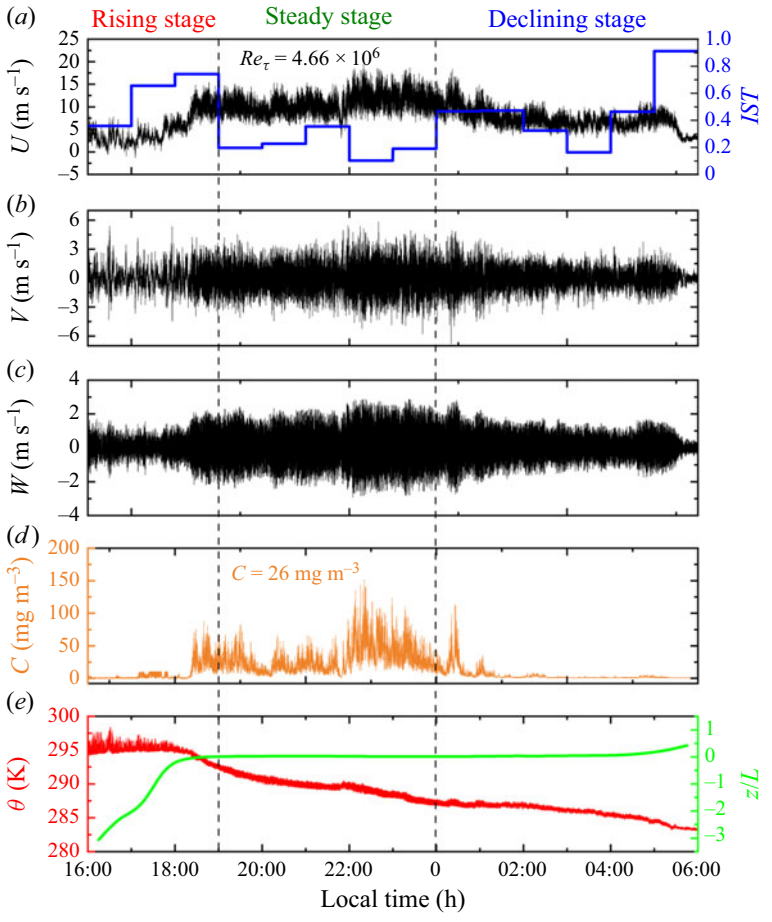

Figure 1. Synchronous measurement data and related parameters at a height of $z = 5$ m over the entire sandstorm process. (*a–c*) Streamwise, spanwise and vertical wind velocities (denoted by U, V and W), where the blue line is the non-stationary index IST; (*d*) PM10 dust concentration (C); (*e*) red line showing the ambient temperature θ and green line showing the Monin–Obukhov thermal stability parameter (z/L).

parameter calculated by the fluctuating vertical velocity and temperature after applying the data processing procedure and is further discussed in § 4.

3. Processing of observational data

3.1. *Non-stationary data processing method*

To obtain the turbulence signals of ASL flows, there are two widely used methods to remove the mean flow. For the steady case, the arithmetic mean of a fixed length velocity time series is usually taken as the mean flow, where the averaging interval of 1 h is widely adopted (Hutchins *et al.* 2012; Wang & Zheng 2016; Liu, He & Zheng 2023). For non-stationary cases, empirical mode decomposition (EMD) (Huang *et al.* 1998) is usually employed to decompose the velocity time series. The intrinsic mode functions (IMFs) and residual term with periods greater than 1 h are taken as the mean flow because fluctuations of period 1 h or less are considered turbulence, while the slower fluctuations are considered part of the mean field (Wyngaard 1992). Using these two methods to extract the mean

flow in figure 1(*a*), it is found that, for the steady stage of the sandstorm, the results are basically the same, being constant with time, while there is a significant difference between these two methods in the rising and declining stages. The mean flow extracted by EMD exhibits remarkable time-varying characteristics (see figure 8*a* in Appendix A). This provides further evidence that the rising and declining stages of the sandstorm involve typical non-stationary flows caused by sharp changes in the atmospheric incoming flow. The stationary method for calculating the steady incoming flow is not appropriate for the non-stationary process.

To perform statistical analysis, it is necessary to divide the turbulence fluctuations extracted by removing the time-varying mean flow in the sandstorm into several segments satisfying the stationarity conditions. Different from the usual segmentation of atmospheric flow with a fixed interval length, an adaptive segmentation method is employed in this study (Liu *et al.* 2022). First, the period of the minimum segment is estimated according to the characteristic time of typical energetic eddies in the outer region of the wall-bounded turbulence, i.e. $\Delta t = 10\delta/U_c$ (where U_c is the convection velocity taken as the local mean). Then, the adaptive segmented length of interval $\Delta T_i = (N_i - 1)\Delta t$, in which $N_i = 1, 2, \ldots$, is determined by checking the stationarity and statistical convergence of the divided segment of data. After applying the adaptive segmentation procedure to the turbulence signals extracted by removing the time-varying mean (non-stationary method), the interval of each segment of the present sandstorm data is 45, 40, 55 and 40 min in the rising stage, and 25, 30, 45, 20, 25, 30, 35, 45, 35, 25 and 45 min in the declining stage. In addition, different degrees of overlap can be set between two adjacent segments to increase the continuity of evolution. The statistical convergence of each segment is confirmed in figures 9 and 10 in Appendix A.

The statistical results, such as turbulent intensity and pre-multiplied energy spectra, obtained with the non-stationary method agree well with those obtained with the stationary method in the steady stage of the sandstorm, suggesting that the non-stationary data processing method can also be applied to stationary data analysis. However, in the rising and declining stages, there are significant differences between the results obtained with the non-stationary and stationary methods (see figures 11–13 in Appendix A). On the one hand, quantitatively, the stationary method overestimates the low-frequency turbulence intensity of the sandstorm, the scale and the kinetic energy fraction of the VLSMs. This is because the stationary method does not remove the gusting or sharp changes in the mean flow, leading to the higher low-frequency energy of the non-stationary system. On the other hand, qualitatively, the stationary method misjudges the attenuation of the structure scale as increasing in the declining stage since the residual gusting or drastic change in the mean field masks the turbulence attenuation in the actual sandstorm decline process.

3.2. *Two-phase flow parameters*

The friction Reynolds number Re_τ is widely used in wall-bounded turbulence and is defined as the ratio of the outer scale δ to the inner viscous scale ν/u_τ, i.e.

$$Re_\tau = \frac{\delta u_\tau}{\nu}. \tag{3.1}$$

The friction velocity u_τ is calculated as $u_\tau = \sqrt{-(\overline{uw})}$ following Hutchins *et al.* (2012) and Li & Neuman (2012), where u and w are the fluctuating streamwise and vertical velocities at $z = 2.5$ m, respectively, and the overbar denotes the time average. The kinematic viscosity ν is estimated based on the barometric pressure and the temperature at the

observation site (Tracy, Welch & Porter 1980). The ASL thickness δ is reasonably adopted as 150 m based on the measurements made with Doppler lidar (Liu *et al.* 2023).

The thermal stability of the data during the sandstorms can be characterized by the Monin–Obukhov stability parameter, which is given as

$$z/L = -\frac{\kappa z g \overline{w\theta'}}{\bar{\theta} u_\tau^3}, \tag{3.2}$$

where $\kappa = 0.41$ is the Kármán constant, g is the gravity acceleration, w and θ' are the fluctuating vertical velocity and temperature after removing the time-varying mean, respectively, $\overline{w\theta'}$ is the average vertical heat flux obtained by the covariance between w and θ' and $\bar{\theta}$ is the average temperature.

The particle mass loading Φ_m is estimated based on the average PM10 dust concentration $\bar{C}$ and the percentage of PM10 (denoted by $P_{d\leq 10\,\mu\mathrm{m}}$) in all sand particles with different sizes (detailed in Liu *et al.* 2023), i.e.

$$\Phi_m = \frac{\Phi_m^{PM10}}{P_{d\leq 10\,\mu\mathrm{m}}} = \frac{\bar{C}}{\rho_f P_{d\leq 10\,\mu\mathrm{m}}}, \tag{3.3}$$

where $\rho_f \approx 1.26\,\mathrm{kg\,m^{-3}}$ is the air density, and Φ_m^{PM10} is the average mass loading of particles with sizes less than 10 µm (i.e. PM10 mass loading). The average PM10 dust concentrations $\bar{C}$ evolving over time at different heights are plotted in figure 2(*a*). The sand particles were collected at different heights (z = 0.9, 2.5, 5, 8.5, 10.24, 14.65, 20.96 and 30 m) during the sandstorm, and the particle size distribution is acquired through analysing these collected sand particles with a commercial standard sieve analyser (MicrotracS3500) (Liu *et al.* 2023). The resulting particle size distribution is shown in figure 2(*b*), and $P_{d\leq 10\,\mu\mathrm{m}}$ at all eight heights is shown in figure 2(*c*).

The Stokes number St represents the relative strength of inertia and diffusion of particles, which is defined as the ratio of the particle relaxation time τ_p to the fluid characteristic time. When the fluid characteristic time is taken as the Kolmogorov time scale τ_η, the corresponding St_η is given as

$$St_\eta = \frac{\tau_p}{\tau_\eta}. \tag{3.4}$$

The particle relaxation time τ_p can be estimated as (Wang & Stock 1993)

$$\tau_p = \frac{\rho_p \bar{d}_p^2}{18\rho_f \nu}, \tag{3.5}$$

where $\rho_d \approx 2650\,\mathrm{kg\,m^{-3}}$ is the particle density and $\bar{d}_p$ denotes the average sand particle size at each height (as shown in figure 2*c*). The Kolmogorov time scale τ_η is calculated as (Pope 2000)

$$\left.\begin{aligned} \tau_\eta &= \frac{\eta^2}{\nu}, \\ \eta^+ &= \left(\kappa z^+\right)^{1/4}, \end{aligned}\right\} \tag{3.6}$$

where η is the Kolmogorov length scale (microscale) and '+' represents the inner-flow scaling normalized with the viscous scale ν/u_τ, i.e. $\eta^+ = \eta u_\tau/\nu$ and $z^+ = z u_\tau/\nu$.

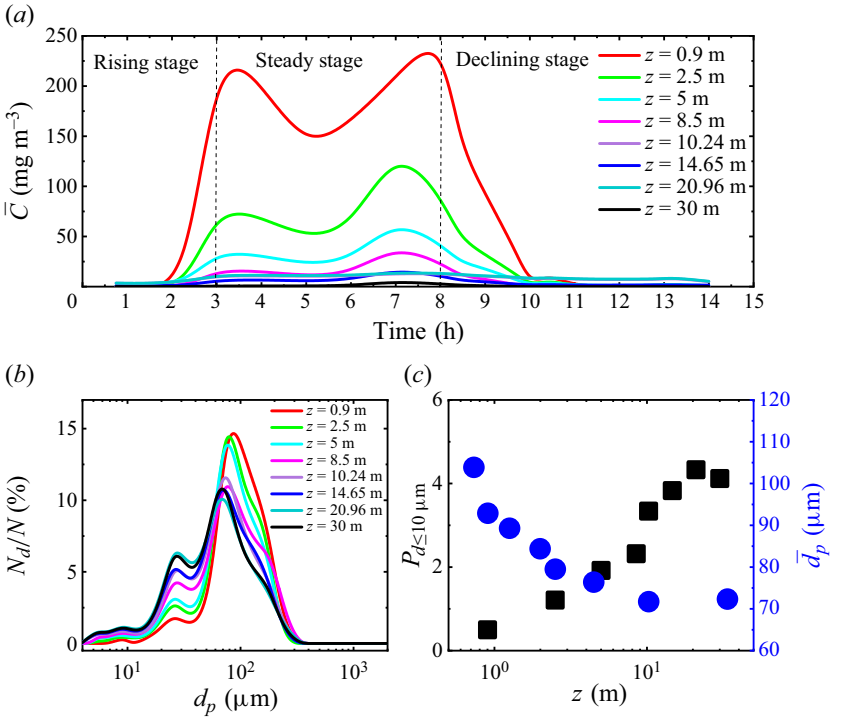

Figure 2. (*a*) Evolution of average PM10 dust concentration $\bar{C}$ over time during the sandstorm process at different heights. (*b*) Sand particle size distribution at different heights, where N_d is the number of sand particles with diameter d and N is the total number of sand particles with different sizes. (*c*) Variations in percentage of PM10 ($P_{d\leq10\,\mu m}$, shown by black squares) and average sand particle size ($\bar{d}_p$, shown by blue circles) with height.

Similarly, when the fluid characteristic time is taken as the viscous time scale ν/u_τ^2, the corresponding St^+ is given as

$$St^+ = \frac{\tau_p u_\tau^2}{\nu}. \tag{3.7}$$

The resulting key fluid and particle parameters related to the particle-laden flow at different stages of the sandstorm are listed in table 1.

4. Evolution of driving factors in the sandstorms

The ASL is a typical convective boundary layer in which the shear turbulence and thermal turbulence coexist (Rao & Narasimha 2006; Nguyen *et al.* 2013; Ding *et al.* 2018; Salesky & Anderson 2018; Tong & Ding 2020). The relative magnitudes of the thermal buoyancy and shear terms can be characterized by the Monin–Obukhov stability parameter z/L defined in (3.2). The Monin–Obukhov length L is often interpreted as the height at which the buoyancy-induced TKE budget (increasing, $L < 0$ or consuming, $L > 0$) is equal to the TKE produced by shear (Obukhov 1946; Monin & Obukhov 1954; Businger & Yaglom 1971; Metzger, McKeon & Holmes 2007; Chamecki *et al.* 2017; Tong & Ding 2020). Based on the Monin–Obukhov length L, the thermal stability of the ASL can be labelled as unstable ($L < 0$), neutral ($|L| \to \infty$) and stable ($L > 0$) stratification. In practice, the ASL with $|z/L| \ll 1$ is considered to be a near-neutral condition. A value of 0.1 is a

	Parameter	Rising stage	Steady stage	Declining stage
Fluid	$\bar{U}$ (m s^{-1})	2.66–9.61	10.27	4.29–9.06
	u_τ (m s^{-1})	0.11–0.20	0.47	0.25–0.49
	ν (m^2 s^{-1})	1.76×10^{-5}–1.78×10^{-5}	1.72×10^{-5}	1.66×10^{-5}–1.69×10^{-5}
	Re_τ	$<3.75 \times 10^6$	4.56×10^6	$<4.63 \times 10^6$
	$\bar{\theta}$ (K)	293.49–295.21	289.65	283.52–287.18
	z/L	−3.06–0.003	0.02	0.02–0.42
Particle	$\bar{C}$ (mg m^{-3})	0.02–0.67	0.73	0.02–0.74
	Φ_m	7.22×10^{-7}–2.67×10^{-5}	2.73×10^{-5}	8.34×10^{-7}–1.46×10^{-5}
	d_p/η	0.03–0.07	0.14	0.09–0.15
	St_η	0.11–0.62	2.18	0.89–2.46
	St^+	9.29–92.98	508.06	152.64–589.73

Table 1. Key two-phase flow parameters relating to the sandstorm data. Here, $\bar{U}$ and $\bar{\theta}$ denote the local average velocity and average temperature at 5 m a height; and d_p/η represents the scale ratio of particles to fluid. The results estimated at $z = 5$ m is provided herein for parameters relating to the height.

threshold commonly used to define near-neutral conditions where turbulence is dominated by shear and the effect of buoyancy can be neglected (Högström 1988; Högström, Hunt & Smedman 2002; Metzger *et al.* 2007; Hutchins *et al.* 2012; Liu, Wang & Zheng 2018; Emes *et al.* 2019; Ayet & Katul 2020). The unstable stratification condition is $z/L < -0.1$, where the effect of buoyancy needs to be taken into account and becomes stronger as the thermal instability increases, and the stable condition is $z/L > 0.1$, where shear turbulence is suppressed.

The Monin–Obukhov stability parameter z/L during the entire sandstorm process in figure 1(*e*) shows that z/L evolves from values less than zero to near zero and then to greater than zero as the sandstorm develops. This indicates that the thermal turbulence is strong in the rising stage of the sandstorm due to the large temperature difference between the air flow of the cold front transit and the warm air at the surface. Over time, the temperature of the upper and lower layers of air gradually mixes evenly, leading to a weakened thermal convection in the steady stage. Finally, in the declining stage, the cold and denser air settles to the surface and the atmosphere is transformed into a stable stratification.

Quadrant analysis is a simple, but quite useful, data-processing technique in the exploration of shear turbulence (Wallace 2016). Thus, to reveal the evolution of the shear-driven turbulence in the sandstorm, figure 3(*a–c*) shows the quadrant analysis of the streamwise and vertical velocity fluctuations in three stages of the particle-laden sandstorm flows. The distribution range and uniformity in each quadrant change with sandstorm evolution. The distribution range of the fluctuating velocity represents the amplitude, and thus a measure of the TKE. Therefore, figure 3(*a–c*) suggests that the sandstorm exhibits a larger TKE in the rising stage because of the superposition of the buoyancy-driven turbulence caused by the strong thermal instability, a slightly reduced TKE in the steady stage since sand emission and transport consume some of the system energy, and a distinctly attenuated TKE in the declining stage due to the suppressed turbulent motions by gravity under stable stratification conditions. In addition, the vortex generated by the shear (hairpin vortex or quasi-streamwise vortex in Townsend 1976) causes the lower velocity fluids to throw up and the higher velocity fluids to sweep down ('ejection' and 'sweep' events in Jeong *et al.* 1997), leading to the streamwise and vertical fluctuating velocities generally distributing over the Q_2 and Q_4 quadrants. Therefore, the relatively

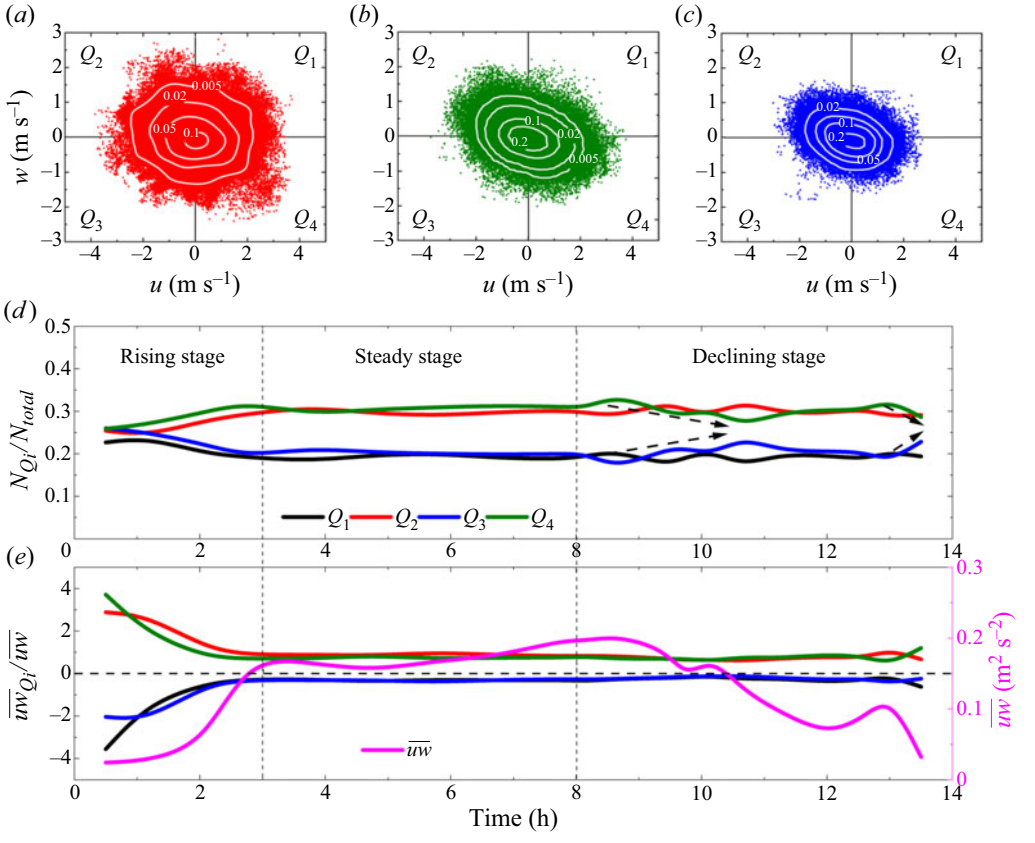

Figure 3. Quadrant distributions of the streamwise and vertical velocity fluctuations (u, w) in different stages of the sandstorm at 5 m height (dot symbols), and the corresponding joint probability density function $P(u, w)$ (white lines). (*a*) Rising stage, (*b*) steady stage, (*c*) declining stage. The evolution of (*e*) the probability of each quadrant event N_{Q_i}/N_{total}, (*e*) the intensity of contributions to the Reynolds shear stress of each quadrant event $\overline{uw}_{Q_i}/\overline{uw}$ and the Reynolds shear stress $\overline{uw}$ with time during the sandstorm. Further evidence from the results of another sandstorm is provided in figure 14 in Appendix B.

uniform quadrant distribution implies weak shear-driven turbulence in the rising stage; the distinct tilt toward the Q_2 and Q_4 quadrants in the steady stage suggests enhanced 'ejection' and 'sweep' events and thus strong shear-driven turbulence; and the weakened tilt in the declining stage indicates attenuated shear turbulence.

Despite the scatter plots of streamwise and vertical fluctuation distributions being visualized for analysing quadrant events, the Reynolds shear stresses cannot be easily estimated. Therefore, to quantitatively analyse the contribution of the quadrant events to the Reynolds shear stress, the evolution of the probability and intensity of each quadrant event are shown in figure 3(*d*,*e*), and the total Reynolds shear stress ($\overline{uw}$) is also plotted in figure 3(*e*). The probability is given as N_{Q_i}/N_{total}, where N_{Q_i} is the number of corresponding quadrant event and N_{total} is the total number of all quadrant events, which represents the occurrence frequency of each quadrant events. The intensity is calculated as $\overline{uw_{Q_i}}/\overline{uw}$, where $\overline{uw_{Q_i}}$ is the Reynolds shear stress generated by each quadrant events and $\overline{uw}$ is the total Reynolds shear stress. At the beginning of the sandstorm, although the intensity of each quadrant event is significant, the probabilities are nearly equal, which results in a small total Reynolds shear stress (as shown by the solid pink line), implying

weak shear-driven turbulence in the rising stage. With the development of the sandstorm, the intensities of the four quadrant events decrease, but the probabilities of the 'ejection' and 'sweep' events reflected by the Q_2 and Q_4 quadrants increase and those reflected by the Q_1 and Q_3 quadrants decrease, which results in a higher Reynolds shear stress, indicating the shear-driven turbulence is enhanced. After full sandstorm development, both N_{Q_i}/N_{total} and $\overline{uw_{Q_i}}/\overline{uw}$ are constant in the steady stage. The probabilities of the four events are approximately 0.19 for Q_1, 0.30 for Q_2, 0.20 for Q_3 and 0.31 for Q_4. This agrees well with the $N_2/N_{total} \approx N_4/N_{total} \approx 0.29$ result previously documented in Katul *et al.* (1997) and $N_2/N_{total} = 0.296$, $N_4/N_{total} = 0.314$ results reported by Li & Bo (2019). The contributions of different quadrant events to the Reynolds shear stress (Q_1, −0.31; Q_2, 0.87; Q_3, −0.30; Q_4, 0.75) are significantly larger than the low-Reynolds-number results (Q_1, −0.1; Q_2, 0.66; Q_3, −0.11; Q_4, 0.52, Nagano & Tagawa 1988), but have a same overall trend, i.e. $Q_2 > Q_4 > Q_1 \approx Q_3$. During the declining stage, as the sandstorm attenuates, although the intensities hardly change, the probabilities of Q_3 and Q_4 are closer, resulting in a decrease in the total Reynolds shear stress; that is, the shear-driven turbulence is weakened. It is noted that the seemingly constant probability from the 11th to 13th hour in the declining stage is attributed to the temporary maintenance of wind velocity, as shown in figure 1(*a*).

In summary, this section indicates that, over the entire sandstorm process, the driving factors evolve from buoyancy-driven thermal turbulence predominating in the rising stage to weakened thermal turbulence but dominant shear-driven turbulence in the steady stage and then to suppressed turbulent motion by enhanced thermal stability.

5. Evolution of the cumulative TKE scaling law in the sandstorms

From the evolution of the driving factors in the sandstorm, it is inferred that the dynamic process of turbulent structures; that is, the generation of primary vortices by kinetic bursts, being stretched into hairpin vortices, aligning coherently to create hairpin vortex packets and thus large- and very-large-scale structures (Townsend 1976; Kim & Adrian 1999; Adrian *et al.* 2000), reflected by the 'ejection' and 'sweep' events in the sand-laden flow change over the different sandstorm stages. To explore the effects of changes in the turbulence driving factors on scaling, this section shows the evolution of the second-order structure function during the sandstorm process.

The second-order streamwise velocity structure function is defined as the second-order statistical moment of the streamwise velocity increment with distance r, i.e.

$$S_{2,u}(r) = [u(x) - u(x+r)]^2, \tag{5.1}$$

which represents the cumulative energy of eddies of size r and less (Davidson, Krogstad & Nickels 2006*a*) and exhibits four scaling ranges (Davidson, Nickels & Krogstad 2006*b*; de Silva *et al.* 2015),

$$S_{2,u}(r) = \begin{cases} z^+(r/z)^2/(15\kappa), & 0 < r \le \eta, \\ M_2(r/z)^{2/3}, & \eta \ll r < z, \\ A + B\ln(r/z), & z < r \ll \delta, \\ C - D\ln(\delta/z), & r \sim \delta. \end{cases} \tag{5.2}$$

At dissipative scales, there is a near balance between the turbulent production (P) and dissipation (ϵ) rates. In the inertial subrange ($\eta \ll r < z$), the scaling behaviour is local isotropy, and the expression of the second-order structure function corresponds to Kolmogorov's two-thirds law. At scales $z < r \ll \delta$ (energy-containing region), the

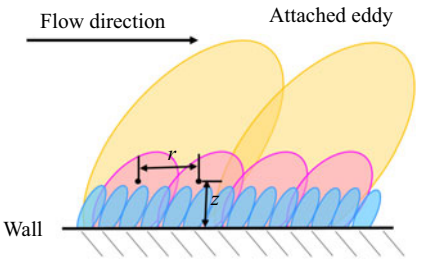

Figure 4. A schematic of the attached eddies. The two points are at a distance z from the wall and are displaced by a distance r in the streamwise direction.

second-order structure function is dominated by inertial-scale eddies and follows logarithmic law. At a scale comparable to the boundary layer thickness, the second-order structure function becomes a constant. In the outer region of the high-Reynolds-number wall turbulence, the very-large-scale coherent structures are dominant. Therefore, the logarithmic behaviour in the energy-containing region is specifically concerned in this study.

According to the Townsend's attached eddy hypothesis (shown as the schematic in figure 4), the flow in the logarithmic layer is filled with wall-attached eddies. Here, the velocity is defined as the sum of the attached-eddy-induced velocity increments (Yang *et al.* 2017; Xie *et al.* 2021), i.e.

$$u(z) = \sum_{i=1}^{N_z} a_i, \tag{5.3}$$

where $u(z)$ is the instantaneous streamwise fluctuation at a distance z from the wall in the logarithmic layer, a_i is the $\delta/2^i$-sized attached-eddy-induced streamwise velocity. The number of wall-attached eddies that contribute to $u(z)$ equals the integral from z to δ of the eddy population density $P(z)$; that is, $N_z = \int_z^\delta P(z)\,\mathrm{d}z$. Because the sizes of the wall-attached eddies scale as their distances from the wall, $P(z)$ is inversely proportional to the distances from the wall z, i.e. $P(z) \sim 1/z$.

The streamwise velocity difference between two points with distance r is written as

$$u(x, z) - u(x + r, z) = \sum_{i=1}^{N_z} \left(a_i - a_i'\right). \tag{5.4}$$

A large-scale attached eddy (coloured yellow in figure 4) contributes the same increment to both the two points and a small-scale attached eddy (coloured blue in figure 4) contributes to neither. Thus, the velocity difference with distance r only contains contributions from intermediate-sized eddies (coloured carmine in figure 4)

$$u(x, z) - u(x + r, z) = \sum_{i=N_r}^{N_z} \left(a_i - a_i'\right), \quad N_r \sim \ln(\delta/r), \tag{5.5}$$

where N_r is the number of wall-attached eddies that contribute to $u(z)$ but their size less than r. Then, a logarithmic scaling of the second-order structure function can be obtained

by squaring both sides of (5.5) and taking the ensemble average

$$\left\langle [u(x,z)-u(x+r,z)]^2 \right\rangle \sim (N_z - N_r)\left(\left\langle a_i^2 \right\rangle + \left\langle a_i'^2 \right\rangle - 2\left\langle a_i a_i' \right\rangle\right)$$
$$\sim (N_z - N_r)\left(\left\langle a^2 \right\rangle - \left\langle aa' \right\rangle\right) \sim N_z - N_r \sim \ln(r/z); \tag{5.6}$$

that is

$$\left\langle [u(x,z)-u(x+r,z)]^2 \right\rangle = A + B\ln(r/z). \tag{5.7}$$

In addition, the derivative of the second-order structure function,

$$\mathrm{d}S_{2,u}(r/z)/\mathrm{d}(r/z) = B\frac{1}{r/z}, \tag{5.8}$$

plays the role of an energy density. The pre-multiplied derivative of the second-order structure function is equal to the parameter B; that is

$$\frac{r}{z}\,\mathrm{d}S_{2,u}(r/z)/\mathrm{d}(r/z) = B, \tag{5.9}$$

which is a measure of the kinetic energy of eddies of size r.

Figure 5(a) presents the second-order structure functions of streamwise velocity fluctuations in different stages of the sandstorm, where black lines represent the theoretical formulas based on stationary atmospheric turbulence (de Silva *et al.* 2015; Chamecki *et al.* 2017; Xie *et al.* 2021). The inset plotted results in log–log scales to better assess the power-law behaviour. There are significant differences in the profiles of the structure function among the different stages. In the steady stage, the profile agrees well with the theoretical formulas of the log–linear law in the energy-containing region and the two-thirds power law in the inertial region. However, in the rising and declining stages, the profiles deviate from the theoretical formula, and the degree of deviation in the energy-containing region becomes increasingly significant with increasing structural scale. This may imply that the existing formula based on stationary atmospheric flows is not suitable for scaling the cumulative energy of eddies on different scales in the non-stationary process of the sandstorm. Although the profiles in non-stationary cases are different from the existing formula, there are still intervals following the predicted log–linear behaviour and two-thirds power law. In the inertial subrange ($r/z < 1$), as shown by the inset in figure 5(a), the profiles of the second-order structure function in log–log scales at different stages are straight, implying a power law. The power-law exponents for the three stages are $p = 0.68 \pm 0.04$, 0.66 ± 0.05 and 0.66 ± 0.04 by fitting the data, which are in general agreement with $p = 2/3$ predicted by the Kolmogorov's two-thirds law (Frisch & Kolmogorov 1995), and also match $p = 0.68$ for the ASL, $p = 0.67$ for a laboratory result (de Silva *et al.* 2015) and $p = 0.68 \pm 0.01$ for the Rayleigh–Bénard convection (Sun, Zhou & Xia 2006). However, in the energy-containing region ($z < r \ll \delta$), the parameter B that represents how quickly the cumulative TKE increases with increasing scale (Townsend 1976; Falkovich 2018) is changed (as shown in figure 5b), where B is obtained from the pre-multiplied derivative of the second-order structure function. Figure 5(b) shows that the pre-multiplied derivatives of the second-order structure function (a measure of the kinetic energy of eddies with scale r, Davidson *et al.* 2006*a*) vs the streamwise length r/z exhibit a plateau at all three stages of the sandstorm, but there are significant differences in the range (representing the interval of the logarithmic law) and magnitude (i.e. the value of B) of the plateau.

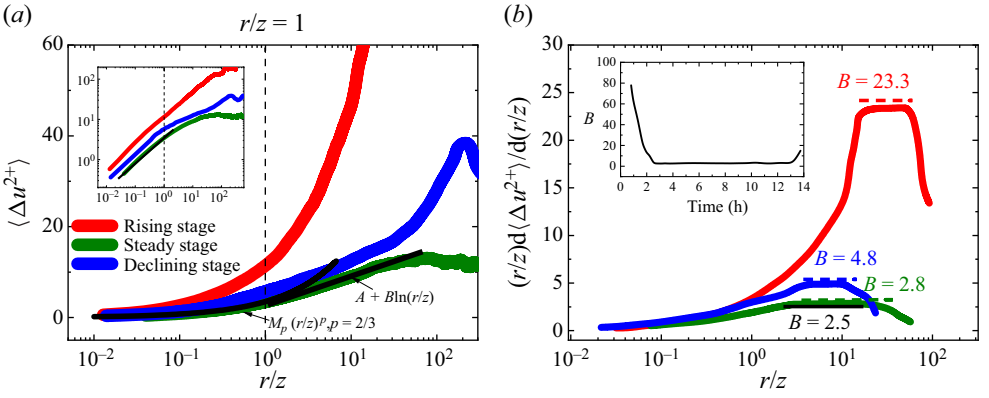

Figure 5. (*a*) Plots of the second-order structure function of the streamwise velocity fluctuations $\langle \Delta u^{2+} \rangle$, the inset shows the results at a log–log scale; (*b*) the corresponding pre-multiplied derivative $(r/z)[\mathrm{d}\langle \Delta u^{2+} \rangle / \mathrm{d}(r/z)]$ vs r/z in the rising (red line), steady (blue line) and declining (green line) stages of the sandstorm at a 5 m height, where the plateau magnitude is the value of B, '+' denotes the inner scaling, $u^{2+} = u^2/u_\tau^2$, $\langle \cdot \rangle$ denotes the time average, black lines represent the theoretical formulas based on the stationary atmospheric flow, $B = 4/3\kappa^{-2/3} \approx 2.5$ (Chamecki *et al.* 2017; Xie *et al.* 2021), $A = 2.95$ and $M_p = 3.12$ (de Silva *et al.* 2015). The illustration shows the evolution of B obtained from the plateau value over time. See figure 15 in Appendix B for the results of another sandstorm.

The plateau range moves left from larger scales of approximately $z \ll r < \delta$ at the right side in the rising stage to $z < r \ll \delta$ in the steady and declining stages, while the plateau magnitude decreases from $B = 23.3$ to 2.8 and then increases slightly to 4.8. These changes suggest that in the rising stage of the sandstorm, in addition to the larger size of the energetic structure, the kinetic energy is also stronger because the scales of the convective structures dominated by thermal turbulence are larger and the energy is mainly concentrated in the larger energetic structures. In the steady stage, both the scale and the kinetic energy decrease. This is because shear-driven turbulence is dominant in this case, and the strong shear not only acts on the surface to generate a new small-scale vortex but also breaks up the large convective structure (Hunt & Morrison 2000; Liu *et al.* 2022), transferring energy to the small scales and thus reducing the kinetic energy of the energetic structures. Especially in the declining stage, the kinetic energy of the energetic structures is slightly enhanced again, although the further length scale decreases. This may be plausible given that the attenuated shear turbulence, especially suppressed by gravity when stably stratified, is unable to generate more small-scale vortices, so that the larger-scale structures cannot retain their coherence, resulting in a scale reduction and refocusing of the energy on these energetic structures due to the absence of small scales.

Specifically, the evolution of the scaling parameter B over time in the inset of figure 5(*b*) shows that B decreases rapidly in the rising stage of the sandstorm, remains virtually unchanged in the steady stage and increases slightly in the declining stage. This indicates that the cumulative TKE increases more quickly with increasing scale in the non-stationary stage of the sandstorm than in the stationary stage, even in the declining stage where the velocity attenuates. Given that $B = 2.8$ in stationary sandstorm flows is close to $B = 2.35{-}3$ in high-Reynolds-number ASL (de Silva *et al.* 2015; Chamecki *et al.* 2017) and $B = 2.5$ in laboratory TBL (Davidson *et al.* 2006*a*,*b*; de Silva *et al.* 2015) and channel (Katul *et al.* 2018; Xie *et al.* 2021) flows at low and moderate Reynolds numbers, it is inferred that the parameter B should be independent of the Reynolds number. This is consistent with the conclusion of de Silva *et al.* (2015) using datasets that span several

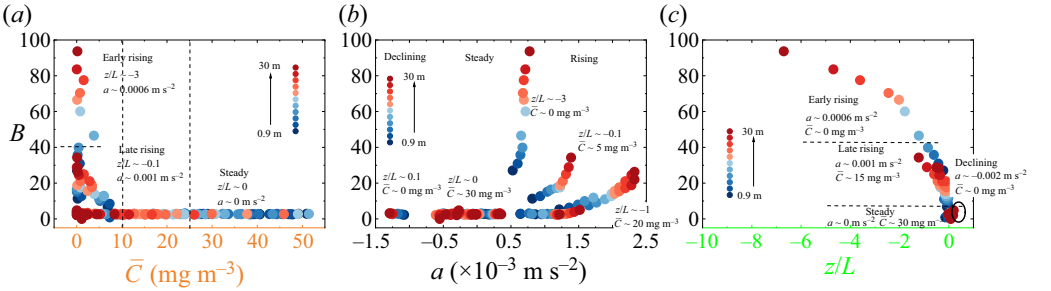

Figure 6. Variations in parameter B of the logarithmic scaling law with the (a) average PM10 dust concentration $\bar{C}$ at different heights, (b) acceleration a of the incoming flow and (c) thermal stability parameter z/L during the sandstorm. See figure 16 in Appendix B for the results of another sandstorm.

orders of magnitude in Reynolds number, up to $Re_\tau \sim O(10^6)$. Therefore, it is not the Reynolds number, but rather the variability in multiple factors (dust concentration, thermal stability and flow acceleration) during the sandstorm that is responsible for the increase in B, that is, the more rapid increase in the cumulative TKE with increasing scale.

Sandstorms as a typical wind-blown-sand two-phase flow, the effect of particles on turbulence during sandstorms needs to be considered because the sand concentration changes dramatically. Therefore, figure 6(a) presents the resulting B at various PM10 concentrations $\bar{C}$. In the sandstorm steady stage with small B, where the acceleration and thermal stability close to zero, B remains almost constant even if $\bar{C}$ varies by an order of magnitude. This indicates that the cumulative TKE scaling law in the energy-containing region is only minimally affected by sand particles in the sandstorm. In the early rising stage, where $\bar{C}$ is close to zero, B changes across an order of magnitude, indicating that the flow acceleration and thermal stability may be the factors contributing to the change in B.

As shown in figure 1(a), in the rising stage, the velocity is increasing and the flow acceleration has a positive value because the local atmosphere gains energy from the cold air mass brought by the cold front. The exhaustion of the energy brought by the cold air mass leads to the reduced wind velocity and flow deceleration in the declining stage. The accelerated flow has previously been confirmed to be a key factor governing turbulence properties. The flow acceleration significantly enhances the near-wall Reynolds shear stresses (Fernholz & Waenack 1998; Piomelli, Balaras & Pascarelli 2000; Joshi, Liu & Katz 2011; Piomelli & Yuan 2013), making the large-scale coherent structures more elongated (Talamelli *et al.* 2002). The flow acceleration also reduces the burst frequency (Kline *et al.* 1967; Ichimiya, Nakamura & Yamashita 1998; Bourassa & Thomas 2009) and thus the number of near-wall cycles (Piomelli *et al.* 2000; Joshi *et al.* 2011). Additionally, the acceleration process affects the Kármán constant (Emadzadeh, Chiew & Afzalimehr 2010; Joshi *et al.* 2011), enhances the turbulence anisotropy (Jung & Chung 2012) and increases the transition Reynolds number (Costantini *et al.* 2016). Therefore, to explore the effects of flow acceleration on the logarithmic scaling law of the second-order structure function, figure 6(b) shows the variation in B with the flow acceleration (denoted as a) during the sandstorm process. The flow acceleration a represents the changing rate of mean wind velocity and is defined as $a = \mathrm{d}U/\mathrm{d}t$. Here, a is estimated from the average changing rate of velocity in the time-varying mean wind flow extracted by EMD in each segment obtained by the adaptive segmentation method. The magnitude of a represents how quickly the sandstorm develops from the beginning to the steady stage and from the steady stage to its end. In addition, the flow acceleration indicates the amount of kinetic energy gain from

the local synoptic system (such as, cold air mass) during the rising stage. The value of a ($\sim O(10^{-3})$) involved in this study, while seemingly small, represents the development time from the beginning (0 m s^{-1}) to the steady stage (10–15 m s^{-1}) of a sandstorm in real nature, which is approximately 3–5 h (approximately 90 % of all 79 sandstorm events with long-term observation), being more rapid than the development time (9 h) of typhoons recorded by Wang *et al.* (2016). The overall trend in figure 6(*b*) suggests an increasingly significant increase in B with a, i.e. B remains unchanged when a is small, whereas the increase in B with a is pronounced at a large value of a. This indicates that the violent acceleration of the flow field changes the energy distribution of the multiscale structures and concentrates the TKE in large-scale energetic structures. Note that the profiles of B varying with a are not well collapsed. This is because the rising stage is accompanied by changes in thermal stability in addition to acceleration.

Therefore, figure 6(*c*) plots the change in B vs the Monin–Obukhov stability parameter z/L for all of the sandstorm data. As expected, the variation in B with z/L is systematic, suggesting that thermal stability is also a key parameter affecting the TKE of energetic structures. Under the near-neutral stratified condition with z/L close to zero, the significant change in B is caused by the incoming flow that still dramatically changes when z/L decreases rapidly to near zero in the rising stage. In the unstable stratified regime with negative z/L, B increases with decreasing stability. This indicates that affected by thermal instability, the kinetic energy of eddies in the energy-containing region is enhanced.

Figure 6 suggests that the turbulent properties are potentially affected by thermal stratification, suspended particles and flow acceleration. However, the three factors vary simultaneously. To disentangle the various effects in a field study, more datasets from long-term observations were selected where only one parameter is different but other parameters are similar, and the results are shown in figure 7. The results obtained from the laboratory experiments (Davidson *et al.* 2006*a*,*b*; de Silva *et al.* 2015), the ASL observations (de Silva *et al.* 2015; Chamecki *et al.* 2017; Katul *et al.* 2018) and theoretical formulas (Chamecki *et al.* 2017; Xie *et al.* 2021) are also included in figure 7 for comparison. Figure 7(*a*) considers the effect of only the PM10 dust concentration on parameter B based on datasets in near-neutral ASLs with steady wind. Although the current ASL results (shown as diamonds) are not well converged (the scatter would be smaller in a controlled laboratory experiment), the overall trend indicates that the parameter B does not change significantly with PM10 concentration $\bar{C}$ and is generally consistent with the existing laboratory and ASL results. In addition, all of these experimental data fluctuate around the theoretical result shown by the red dashed line. It is predictable that the parameter B does not change with $\bar{C}$ when the mass loading (Φ_m) is smaller than 7.78×10^{-4} (corresponding average PM10 dust concentration of 1.96 mg m^{-3}). This condition belongs to the one-way coupling sparse two-phase flow ($\Phi_m < 10^{-3}$) suggested by Elghobashi (1994), Balachandar & Eaton (2010) and Brandt & Coletti (2022), where the particle effects on turbulence are negligible. The result in figure 7(*a*) may provide support for the conclusion obtained from figure 6(*a*).

Figure 7(*b*) plots the individual effect of flow acceleration on the parameter B based on datasets in near-neutral sand-free ASL flows. The results of accelerating and decelerating incoming flow are shown by black solid and hollow circles, respectively. As shown by the black solid circles, the effect is remarkable when the velocity is increasing (with a positive acceleration a); that is, the parameter B increases with increasing a. A parametric equation is fitted to the exponential trend of accelerated flow data to model the variation in B with a and is given as,

$$B = B_0 + 0.06\exp(3180a), \quad a \geq 0, \tag{5.10}$$

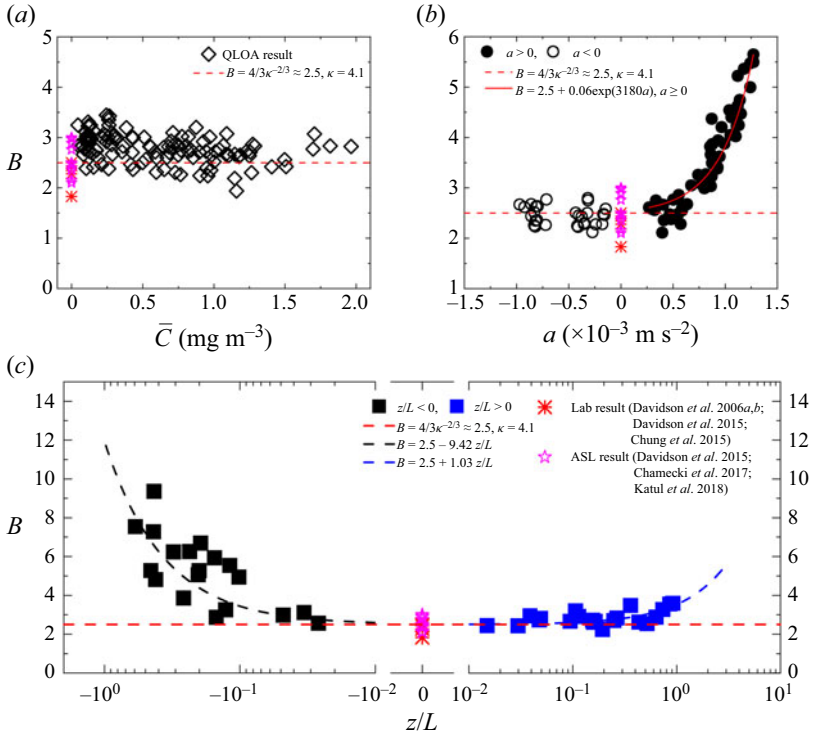

Figure 7. The effect on parameter B by the (a) average PM10 dust concentration $\bar{C}$; (b) acceleration a of the incoming flow, where black solid circles denote the results of accelerating incoming flow and hollow circles are the results of decelerating incoming flow, and the red solid line is the fitting curve for acceleration $a > 0$; and (c) thermal stability parameter z/L, where black and blue squares are the results of unstable and stable surface-layer data, respectively. The black and blue dashed lines are the corresponding fitted curves. In all panels, the red dashed line represents the theoretical formulas based on the stationary atmospheric flow, $B = 4/3\kappa^{-2/3} \approx 2.5$ (Chamecki *et al.* 2017; Xie *et al.* 2021), the red asterisks are the laboratory (LAB) results from Davidson *et al.* (2006*a*,*b*), de Silva *et al.* (2015) and Chung *et al.* (2015) and the carmine stars are the ASL results from de Silva *et al.* (2015), Chamecki *et al.* (2017) and Katul *et al.* (2018).

where $B_0 = 2.5$ is the theoretical result. When the flow is stationary (with an acceleration of $a = 0$), the functional form of the fitted equation (5.10) approaches the invariant value of the parameter B and is consistent with the existing results, while it depicts an increasing B at high a. It is well known that the increase in wind velocity is attributed to the local atmospheric system gaining energy from the environment. Energy cascade theory (Richardson 1922) suggests that large-scale turbulence structures transfer kinetic energy gained from the mean flow field to small-scale turbulence structures, and the bispectrum analysis during sandstorm by Liu *et al.* (2022) suggested that large-scale coherent structures gain energy from nonlinear interactions in the rising stage. Therefore, a higher acceleration a indicates that large-scale turbulence structures in the local atmospheric system gain more kinetic energy from the mean flow field, which leads to an increase in B because it is a measure of the kinetic energy of large structures in the energy-containing region. Meanwhile, flow acceleration increases the Reynolds shear stress at the near-wall surface (Piomelli *et al.* 2000; Joshi *et al.* 2011), resulting in an increase in the velocity gradient and thus the streamwise spacing between different hairpin vortices in the hairpin vortex packet that form the large-scale coherent structure, consequently increasing the scale of the large-scale structure (Adrian *et al.* 2000; Volino 2020). This provided evidence

supporting the larger size of the energetic structure in the rising stage of the sandstorm shown in figure 5(*b*). However, for negative acceleration a, the effect of decelerated flow on parameter B is not significant, as shown by the hollow circles in figure 7(*b*).

The effect of stratification stability on the parameter B is shown in figure 7(*c*) based on sand-free ASL flows with steady wind. As expected, the parameter B increases with decreasing stability (increasing $-z/L$), and the variation follows an approximately linear increase in the unstable regime, as shown by black squares. Under stable conditions, a few cases show a slight linear increase in the parameter B with increasing stability, as shown by blue squares. In the near-neutral ASL, the parameter B results agree well with the existing results shown by red asterisks, carmine stars and red dashed lines in figure 7(*c*). The linear trend is fitted by an empirical correlation to model the variation in the parameter B with z/L and is given as

$$B = \begin{cases} B_0 + 1.03z/L, & z/L \geq 0, \\ B_0 - 9.42z/L, & z/L < 0. \end{cases} \tag{5.11}$$

The self-organized state of multiscale turbulent structures shows a stronger response to unstable conditions than to the stable conditions. A probable interpretation is that buoyant currents shred the synoptic-scale structures into large turbulence structures and further break those structures into small-scale structures (Hunt & Morrison 2000; Lotfy *et al.* 2019; Liu *et al.* 2022), which may cause the energy of large-scale structures to be more significant, that is, the cumulative TKE increases more rapidly with increasing scale in the energy-containing region. The enhanced energy fraction of large-scale structures under unstable conditions is also observed in other ASL measurements and numerical simulations (Kaimal *et al.* 1972; Feigenwinter, Vogt & Parlow 1999; Kim & Park 2003; Salesky *et al.* 2013; Banerjee *et al.* 2015; Lotfy *et al.* 2019; Brilouet *et al.* 2020; Liu *et al.* 2022). The slight increase in the parameter B in stably stratified ASLs indicates a focus of energy in the energetic structures, although the turbulence is suppressed by stable thermal conditions, providing further evidence supporting the results in figure 5(*b*).

6. Concluding remarks

Turbulence fluctuating data are extracted from the velocity time series over the entire sandstorm process by removing the time-varying mean flow with EMD and then the adaptive segmented processing is employed to ensure stationarity and statistical convergence. Statistical analyses of these turbulence signals indicate that thermal turbulence and shear turbulence exhibit a competitive evolutionary process in the rising and declining stages of the sandstorm due to the non-stationarity of sand-laden atmospheric turbulence. That is, the driving factor transitions from the dominant thermal turbulence in the rising stage to the weakened thermal turbulence and dominant shear turbulence in the steady stage and then to the suppressed turbulence motion in the declining stage due to the enhanced thermal stability.

With the evolution of this driving factor, the self-organized state of multiscale structures in the energy-containing region of the sand-laden turbulence also changes significantly as the sandstorm evolves. The logarithmic scaling law of cumulative TKE in the non-stationary rising and declining stages differs significantly from the existing theoretical results. The growth rate of the cumulative TKE in non-stationary stages is much higher than that in the middle stage of sandstorms with steady flow, and the scale of the energetic structures is larger in the rising stage and shorter in the declining stage. This suggests that the structural characteristics in the sandstorm process undergo an evolutionary process: at the beginning the sandstorm, the energy is mainly concentrated in larger energetic

structures. Later on, as the sandstorm develops, the scale and kinetic energy of these structures is reduced because energy is transferred to smaller-scale vortices generated by strong shear. Eventually, at the end of the sandstorm, the energy re-focus on the shorter energetic structure because the suppressed shear leads to discontinuation of the generation of small-scale vortices and the difficulty in maintaining large-scale vortices.

By investigating the effects of independent environmental factors, it is found that the increase in the rate of increase in the cumulative TKE in the rising stage of the sandstorm is mainly caused by the flow acceleration (non-stationarity of the flow) and thermal instability, while it is due to the stable stratification in the declining stage. The influence of PM10 particles is negligible throughout the sandstorm process.

Funding. This study was supported by grants from the National Natural Science Foundation of China (92052202 and 12372217). The authors would like to express their sincere appreciation for the support.

Declaration of interests. The authors report no conflict of interest.

Author ORCIDs.
Hongyou Liu https://orcid.org/0000-0002-2444-543X;
Yanxiong Shi https://orcid.org/0000-0002-6412-8332;
Xiaojing Zheng https://orcid.org/0000-0002-6845-2949.

Appendix A. Details of the non-stationary data processing method

A.1. *Non-stationary data processing method*

In this appendix, we present the details of the non-stationary data processing method mentioned in § 3.1, and the resulting statistical results are compared with those of the stationary method.

The physical quantities in the turbulent field have the characteristics of random functions. That is, within a single experiment, physical quantities are irregular in space and time. However, once several experiments are performed under the same working conditions, the results obtained by arithmetic mean using multi-samples are deterministic. Therefore, the statistical average method is the most basic method to deal with turbulence.

According to the law of large number, statistical analysis requires a large number of samples for the ensemble average; taking the time series of streamwise velocity as an example

$$E\left[U\left(t\right)\right]=\lim_{N\to\infty}\frac{1}{N}\sum_{i=1}^{N}U_i(t). \tag{A1}$$

However, in practice, it is often difficult to acquire a large number of repeated experiments for obtaining the ensemble average. Alternatively, the time average is easier to achieve because it is convenient to perform continuous measurement in time at a fixed point in an experiment. This requires a stationary random process with ergodicity, whose time average (observation time is long enough) of any sample function approaches its statistical ensemble average, i.e.

$$P\left\{E[U(t)]=\overline{U(t)}=\lim_{\Delta T\to\infty}\frac{1}{\Delta T}\int_{t_0}^{t_0+\Delta T}U(t)\,\mathrm{d}t\right\}=1, \tag{A2}$$

where the overbar represents the time average, ΔT is the period of time and t_0 is the initial time. For the steady case, to acquire ergodic (statistically convergent) fluctuating turbulence signals of ASL flows, the observational data are usually divided into multiple

hourly time series following the standard practice in the analysis of ASL data (Wyngaard 1992; Hutchins *et al.* 2012), and the turbulence fluctuations are obtained by removing the arithmetic mean from the data. The stationary data processing procedure is detailed in Wang & Zheng (2016) and is consistent with Hutchins *et al.* (2012) and Liu *et al.* (2023). However, for the non-stationary case, the arithmetic mean of a fixed length time series may be inapplicable due to the time-varying characteristics. Therefore, the existing stationary data processing methods relating to the time average cannot be directly applied to non-stationary signal processing.

The Cramer decomposition theorem indicates that any time series can be decomposed into the sum of deterministic trend component and stationary zero mean fluctuating component. For a random time series, as long as one of the corresponding deterministic and random effects is non-stationary, the time series will be non-stationary. Therefore, the analysis of non-stationary random signals should start from these two aspects. Inspired by this theorem, a non-stationary data processing method based on removing the time-varying mean flow and adaptive segmented stationary is employed.

The non-stationary wind velocity series can be considered an ergodic stochastic process composed of a time-varying mean flow reflecting the overall trend and three fluctuating components of streamwise, spanwise and vertical velocity (Chen & Xu 2004; Wang *et al.* 2016). The gusting or drastic changes in mean flow during the sandstorm rising and declining stages are the main contributors to the non-stationarity, whereas the turbulence information concerned is contained in the fluctuating components. Therefore, it is necessary to remove time-varying mean flow from the wind velocity signals, where the key issue is how to extract an appropriate time-varying mean flow from a wind time history recorded. The EMD, as an adaptive signal processing technique, reduces the artificial selection of parameter because it is based on the local characteristics of data (Huang *et al.* 1998). Therefore, EMD is employed to extract the time-varying mean flow in this study. The EMD can decompose a nonlinear and non-stationary time series into a finite number of component signals called IMFs and a residual term through an adaptive algorithm; that is, a non-stationary wind velocity series $U(t)$ can be expressed as the sum of IMFs and the residual term

$$U(t) = \sum_{i=1}^{n} \mathrm{IMF}_i(t) + r_n(t), \tag{A3}$$

where n is the number of IMFs and $r_{n(t)}$ is the residual term. The previous analysis of atmospheric flow data suggested that the fluctuations with period of the order of 1 h or less are considered as turbulence, while slower fluctuations are part of the mean field (Wyngaard 1992). Therefore, the residual term and IMFs with average fluctuation periods greater than 1 h are taken as the time-varying mean flow

$$\bar{U}(t) = r_n(t) + \sum_{i=M}^{n} \mathrm{IMF}_i \Big|_{\bar{T} \geq 1h}, \tag{A4}$$

where M is the first IMF component with a period greater than 1 h. Then, the turbulence fluctuations can be extracted from the wind velocity signals by removing the time-varying mean flow, i.e.

$$u(t) = U(t) - \bar{U}(t). \tag{A5}$$

The time-varying mean flow extracted by EMD is compared with the hourly arithmetic mean, as shown in figure 8(*a*). As expected, there are significant differences between

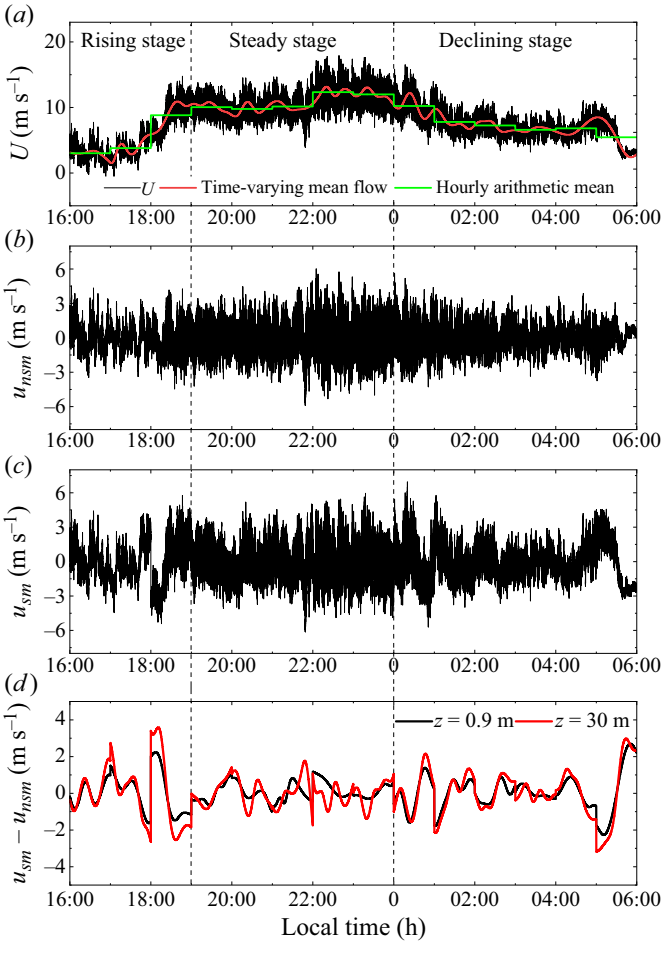

Figure 8. (*a*) Comparisons of the time-varying mean flow and hourly arithmetic mean flow at $z = 5$ m, where the black line is the streamwise wind velocity time series, the red line is the time-varying mean flow obtained by EMD and green line is the hourly arithmetic mean. (*b*) Turbulence fluctuations (u_{nsm}) extracted by removing the time-varying mean flow with EMD at $z = 5$ m. (*c*) Velocity fluctuations (u_{sm}) extracted by removing the hourly arithmetic mean at $z = 5$ m. (*d*) Residual fluctuations relating to the mean field ($u_{sm} - u_{nsm}$) at $z = 0.9$ m (black line) and 30 m (red line).

these two methods in the rising and declining stages. The mean flow extracted by EMD exhibits remarkable time-varying characteristics. Compared with the turbulence fluctuations extracted by removing the time-varying mean flow with EMD in figure 8(*b*), the result obtained by removing the hourly arithmetic mean remains a part of fluctuations relating to the mean field in the turbulence signal (as shown in figure 8*c*), and these residual fluctuations are more predominant with height (as shown in figure 8*d*). The residual fluctuation intensity accounts for 42 % ($(u_{sm} - u_{nsm})/u_{sm} \times 100\,\%$, where u_{nsm} and u_{sm} denote the fluctuations extracted by removing the time-varying mean and hourly arithmetic mean, respectively) of the total intensity in the rising stage, 6 % in the steady stage, and 39 % in the declining stage, respectively. Therefore, the stationary method for calculating the steady incoming flow is not appropriate for the non-stationary processes of sandstorms.

The time-varying characteristics of non-stationary signals may be reflected not only in the mean field, but also in the turbulence fluctuations $u(t)$. For a non-stationary random process $u(t)$, if there is a set of instant points in the interval $[a, b]$

$$\left.\begin{aligned} a = t_0 < t_1 < t_2 < \cdots < t_n = b, \\ \Delta t_i = t_{k+1} - t_k, \quad t_k \leqslant \tau_k \leqslant t_{k+1}, \quad k = 1, 2 \ldots, n, \end{aligned}\right\} \tag{A6}$$

making the time series $\{u(t_k + 1), \ldots, u(t_{k+1})\}$ stationary, then $u(t)$ is piecewise stationary. Each stationary segment can be described by stationary random signal models (Djuric, Kay & Boudreaux-Bartels 1992; Lavielle 1998). Segmentation of random processes is widely used in the analysis and processing of non-stationary signals. For example, the averaging interval is usually taken as 1 h in typhoon signal analysis (Chen & Xu 2004; Wang *et al.* 2018), 30 min in thunderstorm signal analysis (Schulz & Sanderson 2004), 10 min in wind load analysis of building (Tamura *et al.* 1996; Wang *et al.* 2016) and 1 h or 10 min for the analysis of wind field above ocean (Cheynet, Jakobsen & Obhrai 2017; Mahrt *et al.* 2020). These averaging intervals are empirical and cannot guarantee that every segment of data satisfies the stationarity condition (Chen & Xu 2004). Moreover, a fixed length may defeat the purpose of segmentation (Hassanpour, Shahiri & IEEE 2007; Azami *et al.* 2013). Therefore, different from the usual segmentation of atmospheric flow with a fixed interval length, an adaptive segmentation method is employed in this study to divide the turbulence fluctuations extracted by removing the time-varying mean flow in the sandstorm into several segments satisfying the stationarity conditions (Liu *et al.* 2022).

A data segment that can be used to study turbulence should contains at least one typical energetic vortex convective period. In the outer region of the wall-bounded turbulence, very-large-scale coherent structures with lengths up to 10δ have been verified to be an important and perhaps dominant feature (Hutchins & Marusic 2007). Therefore, the period of the minimum segment Δt is estimated according to the characteristic time of typical energetic eddies, i.e. $\Delta t = 10\delta/U_c$ (where U_c is the convection velocity taken as the local mean). On this basis, taking the stationary data condition of $IST < 30\,\%$ (Foken *et al.* 2004) as a threshold, iterations are performed to extend the period such that $u(N_i\Delta t)$ does not satisfy the stationary data condition while $u\{(N_i - 1)\Delta t\}$ satisfies the condition. Then, the adaptive segmented stationary data are taken as $u(\Delta T_i) = u\{(N_i - 1)\Delta t\}$. Repeating the above steps, a non-stationary signal can thus be divided into several segments of stationary signals

$$u(t) = \{u_1(\Delta T_1), u_2(\Delta T_2), \ldots, u_i(\Delta T_i), \ldots, u_m(\Delta T_m)\}, \tag{A7}$$

where $\Delta T_i = (N_i - 1)\Delta t$ and $t = \Delta T_1 + \Delta T_2 + \cdots + \Delta T_m$. In addition, different degrees of overlap can be set between two adjacent segments to increase the continuity of evolution. To ensure ergodicity, it is prudent to confirm statistical convergence. The Ogive analysis describes the probability distribution of a real random variable, which can be used to test the statistical convergence of data. The segment of data is statistically convergent when the cumulative probability distribution of fluctuating velocity satisfies

$$F_U(U_{th})|_t = P(U < U_{th})|_t = F_U(U_{th})|_{t+\Delta t}, \tag{A8}$$

where U_{th} denotes the threshold wind speed.

After applying the adaptive segmentation procedure to the turbulence signals extracted by removing the time-varying mean, the intervals of each segment of the present sandstorm data are 45, 40, 55 and 40 min in the rising stage, and 25, 30, 45, 20, 25, 30, 35, 45, 35, 25 and 45 min in the declining stage. The Ogive analysis is performed on each segment in the

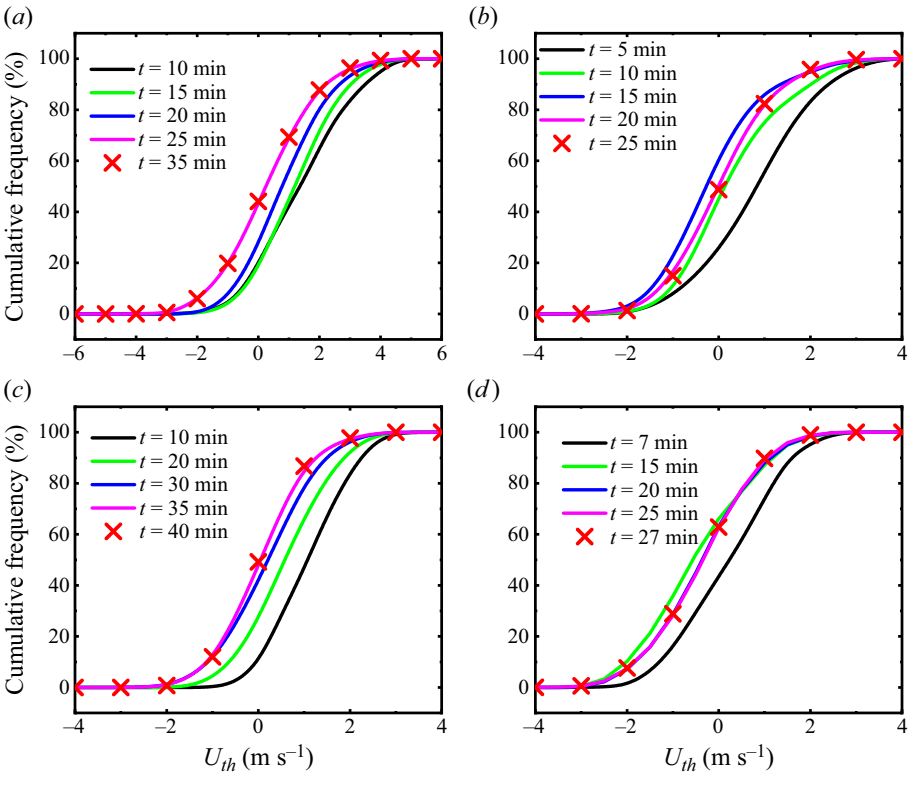

Figure 9. The duration of the rising stage in the sandstorm process selected in this work is 3 h and it is divided into 4 four segments, with time intervals of 45, 40, 55 and 40 min. The cumulative frequencies of these segments for streamwise velocity fluctuations at $z = 5$ m are shown in (*a–d*).

rising and declining stages and the result are shown in figures 9 and 10, respectively. After reaching a certain length, the cumulative probability distribution of each segment will not change with the increasing length. This indicates that each segmented turbulence signal satisfies the statistical convergence and can be used for subsequent statistical analysis.

A.2. *Comparison with the stationary data model*

Comparisons of the statistical results obtained with the non-stationary method and those obtained with the stationary method are provided in this sub-section. It is noted that this subsection pays attention to the difference between the results of the two methods, while the evolution of these results over time or the difference between different stages of sandstorm can be found in Liu *et al.* (2022). First, the streamwise turbulent intensity is shown in figure 11, where figure 11(*a*) plots the evolution of the streamwise turbulent intensity normalized by the friction velocity $\overline{uu}/u_\tau^2$ over time during the sandstorm, and figure 11(*b*) shows variations in the energy fraction contributed by VLSMs to the total kinetic energy with the outer-scaled wall-normal distance. It is seen in figure 11(*a*) that in the rising and declining stages of the sandstorm, the stationary method overestimates the turbulence intensity (with an average of approximately 20 % and a maximum of up to 73 %) compared with the non-stationary method. This is because the stationary method remains a part of low-frequency fluctuations related to the mean field in the turbulence signal, and the residual fluctuation intensity accounts for a large proportion of

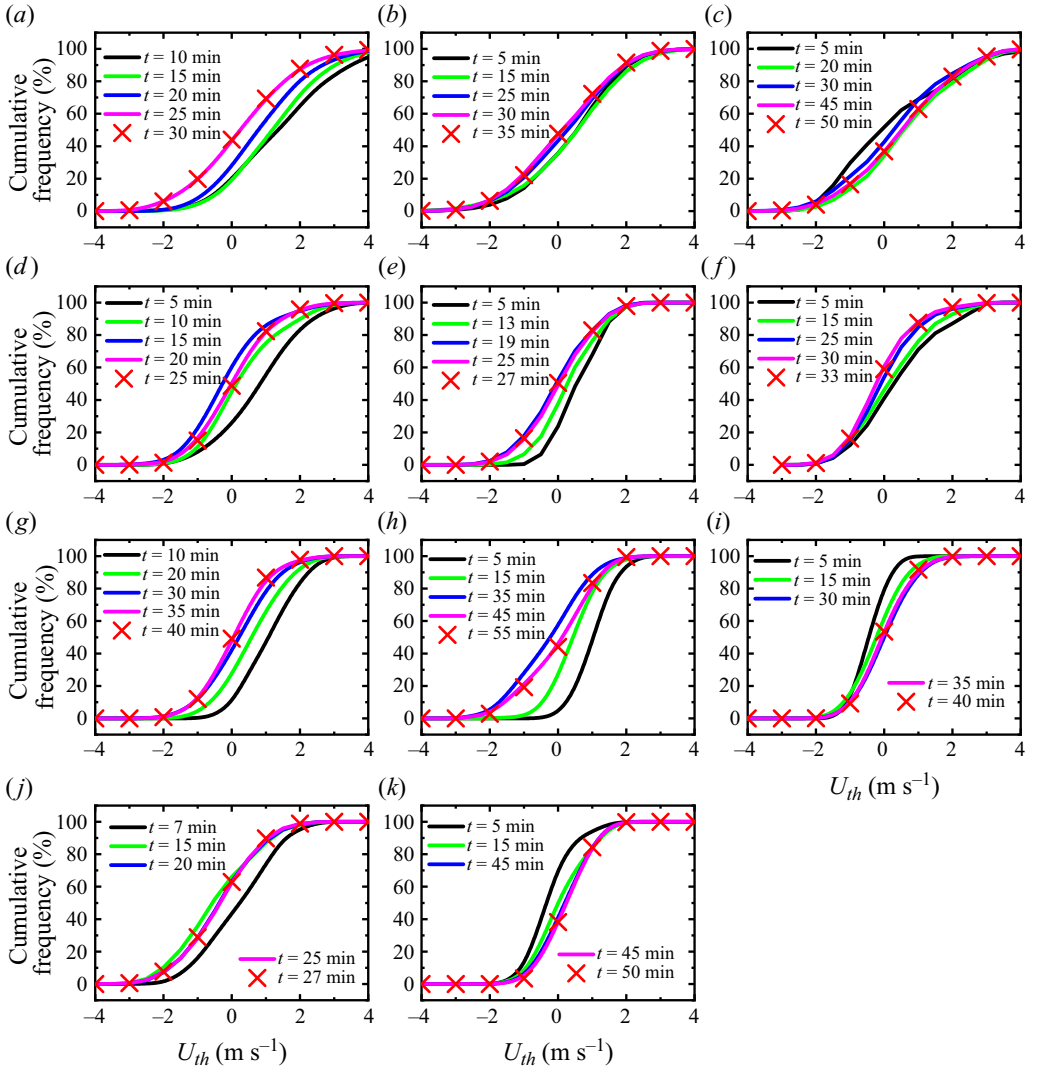

Figure 10. The declining stage of the sandstorm lasts 6 hours and is divided into 11 segments with time intervals of 25, 30, 45, 20, 25, 30, 35, 45, 35, 25 and 45 min. The cumulative frequencies of these segments for streamwise velocity fluctuations at $z = 5$ m are shown in (*a–k*).

the total intensity (as mentioned in the descriptions of figure 8). In addition, the residual low-frequency fluctuations also result in the overestimated energy fraction of the VLSMs, as shown in figure 11(*b*). The variations in the energy fraction with the wall-normal distance and the differences between the three different stages of the sandstorm are detailed in Liu *et al.* (2022).

Second, figure 12 shows pre-multiplied energy spectra of the streamwise velocity fluctuations at different stages of the sandstorm to gain insight into the distribution of energy between multiscale turbulent motions. As expected, the most striking aspect is the significantly overestimated energy obtained with the stationary method in the lower wavenumber region in the rising and declining stages. This may provide evidence for the

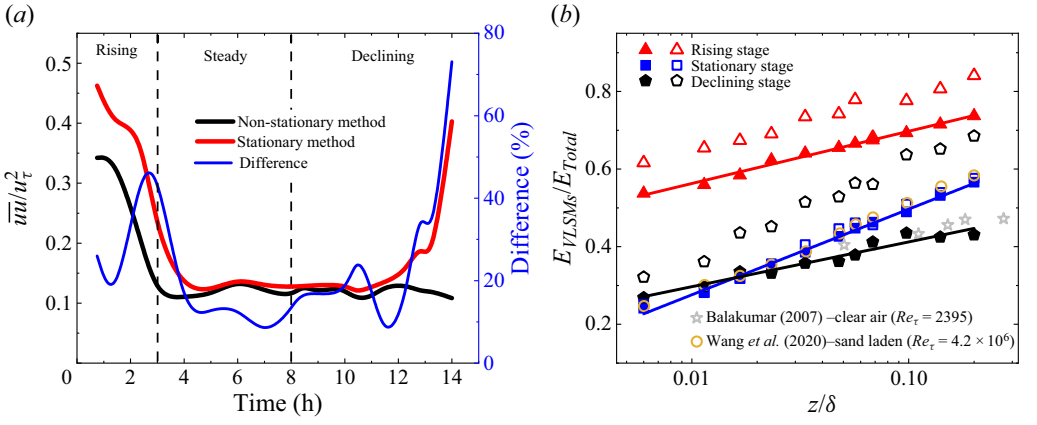

Figure 11. Statistical results of the streamwise turbulent intensity: (*a*) evolutions of the streamwise turbulence intensity normalized by the friction velocity $\overline{uu}/u_\tau^2$ with time during the sandstorm at 5 m height, where the black and red solid lines represent the result of non-stationary and stationary method, respectively; the blue line is the deviation between the results of non-stationary and stationary method; (*b*) variations in the energy fraction contributed by VLSMs to the total streamwise TKE with outer-scaled height z/δ at different stages of the sandstorm, where the filled symbols are results obtained with the non-stationary method and hollow symbols are results obtained with the stationary method; the previously documented laboratory TBL results at $Re_\tau = 2395$ (Balakumar & Adrian 2007) and the sand-laden atmospheric stationary flow results at $Re_\tau = 4.2 \times 10^6$ (Wang, Gu & Zheng 2020) are also included in the figure for comparison.

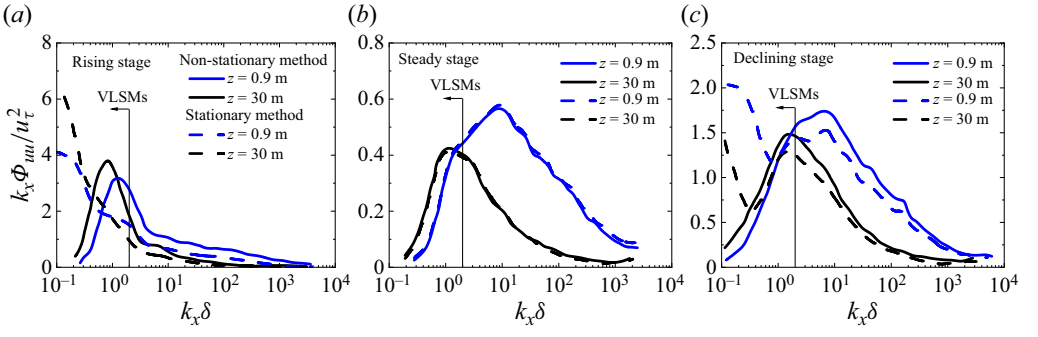

Figure 12. Pre-multiplied spectra of streamwise velocity fluctuations vs streamwise wavenumber during the sandstorm process at heights of 0.9 and 30 m: (*a*) rising stage, (*b*) steady stage and (*c*) declining stage, where the dashed and solid lines represent the results obtained with the stationary method and non-stationary method, respectively.

plausible explanation that the residual low-frequency fluctuations by removing the hourly arithmetic mean cause the turbulence intensity to be overestimated.

Third, to compare the length scale of the most energetic structure estimated by these two methods, the wavelength corresponding to the distinct peak in the pre-multiplied energy spectra is extracted. The resulting most energetic structural scale at different heights during the entire sandstorm process is plotted in figure 13. At the beginning of the sandstorm, with the intrusion of cold air, strong convection occurs due to the interaction between cold and warm air. The small changes in the incoming flow result in the negligible difference in the most energetic structural scale obtained with the two methods. As the sandstorm develops, the rapid increase in wind velocity enhances the non-stationarity of the flow. The gusting or drastic changes in the mean field (i.e. synoptic-scale structures) are incorrectly regarded

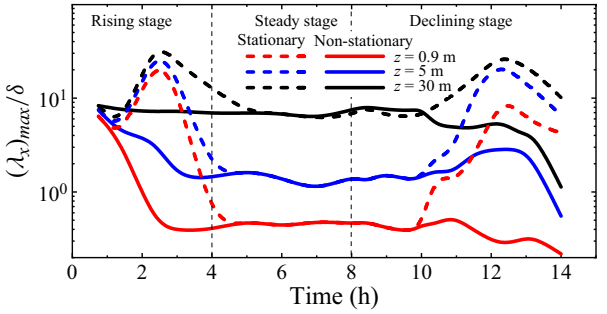

Figure 13. Evolution of the outer-scaled wavelength $(\lambda_x)_{max}/\delta$ corresponding to the distinct peak in the pre-multiplied energy spectra with time at heights of 0.9, 5 and 30 m in the entire sandstorm process, where the solid line and dashed line represent the results obtained with the non-stationary and stationary method, respectively.

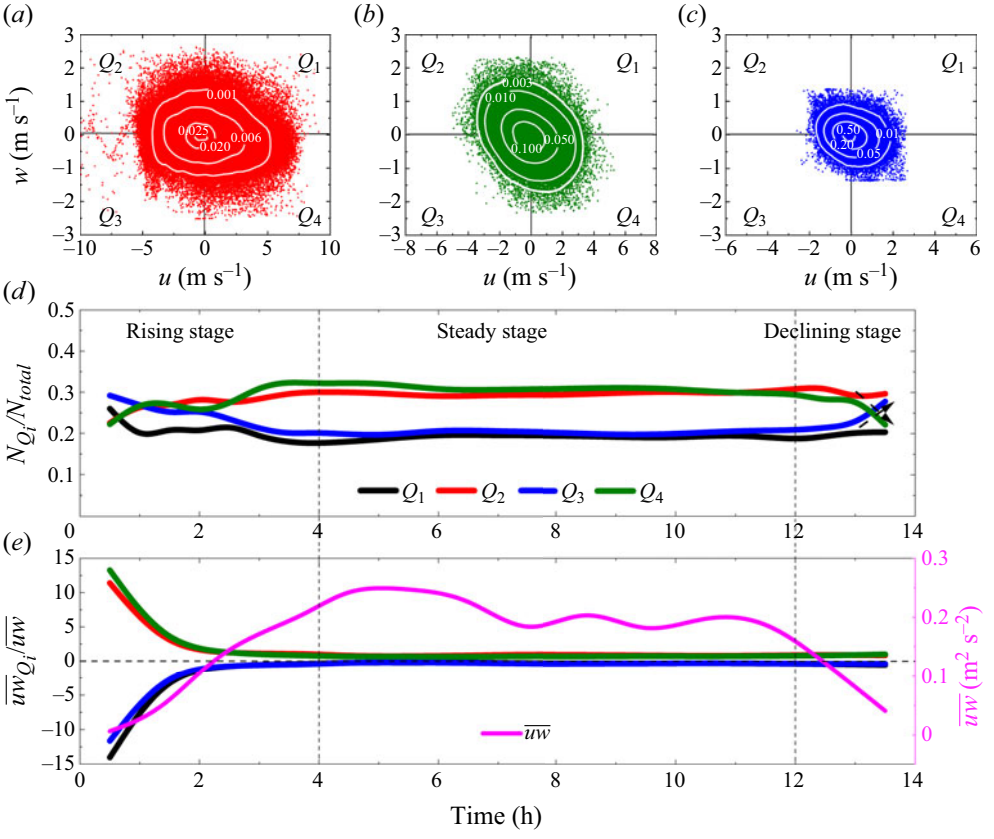

Figure 14. Quadrant distributions of the streamwise and vertical velocity fluctuations (u, w) in different stages of the sandstorm at 5 m height (dot symbols), and the corresponding joint probability density function $P(u, w)$ (white lines). (*a*) Rising stage, (*b*) steady stage, (*c*) declining stage. The evolution of (*e*) the probability of each quadrant event N_{Q_i}/N_{total}, (*e*) the intensity of contributions to the Reynolds shear stress of each quadrant event $\overline{uw}_{Q_i}/\overline{uw}$ and the Reynolds shear stress $\overline{uw}$ with time during the sandstorm.

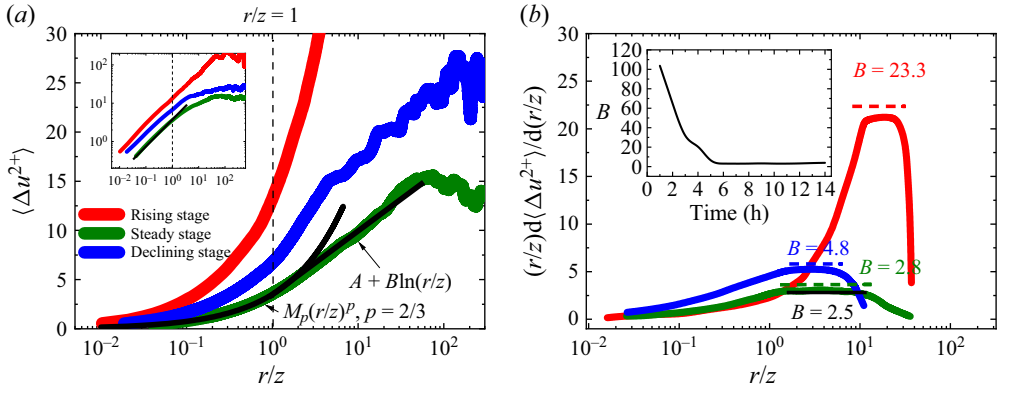

Figure 15. (*a*) Plots of the second-order structure function of the streamwise velocity fluctuations $\langle \Delta u^{2+} \rangle$, where the inset shows the results at a log–log scale; (*b*) the corresponding pre-multiplied derivative $(r/z)[\mathrm{d}\langle \Delta u^{2+} \rangle / \mathrm{d}(r/z)]$ vs r/z in the rising (red line), steady (blue line) and declining (green line) stages of the sandstorm at a 5 m height, where the plateau magnitude is the value of B, '+' denotes the inner scaling, $u^{2+} = u^2/u_\tau^2$, $\langle \cdot \rangle$ denotes the time average, the black lines represent the theoretical formulas based on the stationary atmospheric flow, $B = 4/3\kappa^{-2/3} \approx 2.5$ (Chamecki *et al.* 2017; Xie *et al.* 2021), $A = 2.95$ and $M_p = 3.12$ (de Silva *et al.* 2015). The illustration shows the evolution of B obtained from the plateau value over time.

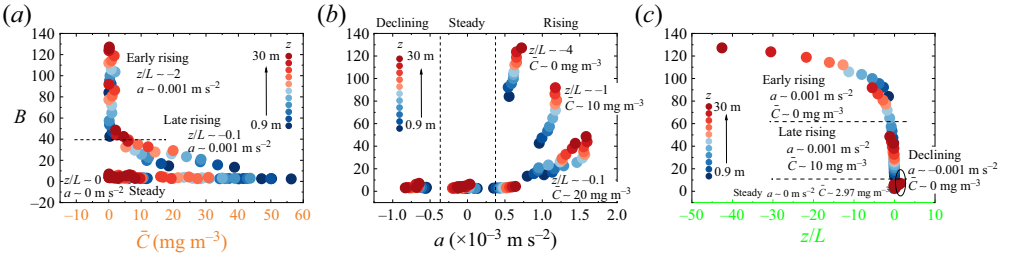

Figure 16. Variations in parameter B of the logarithmic scaling law with the (*a*) average PM10 dust concentration $\bar{C}$ at different heights, (*b*) acceleration a of the incoming flow and (*c*) thermal stability parameter z/L.

as the most energetic turbulent structure determined with the stationary method, which results in a significant overestimation of scale in the rising stage. After full development, the wind velocity is basically stable. For stationary flow, the results obtained with the non-stationary method agree well with those obtained with stationary method. At the end of the sandstorm, with the departure of the cold air mass, the energy is gradually exhausted, which leads to a decrease in the wind velocity. Thus, flow structures, especially large structures, are difficult to maintain. However, the stationary method misjudges the attenuation of the structure scale as increasing in the declining stage since the residual gusting or drastic changes in the mean field mask the turbulence attenuation.

Appendix B. Further evidence supporting the present results from another sandstorm

To verify the reliability of the results described in the main text, this section provides results from other sandstorm data (starting at 13:00 local time on 16 April 2016 and ending at 03:00 on 17 April 2016) available in Liu *et al.* (2022), as shown in figures 14–16.

References

Ackerman, S.A. & Cox, S.K. 1989 Surface weather observations of atmospheric dust over the southwest summer monsoon region. *Meteorol. Atmos. Phys.* **41**, 19–34.

Adrian, R.J., Meinhart, C.D. & Tomkins, C.D. 2000 Vortex organization in the outer region of the turbulent boundary layer. *J. Fluid Mech.* **422**, 1–54.

An, S., Sin, H.H. & DuBow, M.S. 2015 Modification of atmospheric sand-associated bacterial communities during Asian sandstorms in China and South Korea. *Heredity* **114**, 460–467.

Ayet, A. & Katul, G.G. 2020 Scaling laws for the length scale of energy-containing eddies in a sheared and thermally stratified atmospheric surface layer. *Geophys. Res. Lett.* **47** (23), e2020GL089997.

Azami, H., Sanei, S., Mohammadi, K. & Hassanpour, H. 2013 A hybrid evolutionary approach to segmentation of non-stationary signals. *Digit. Signal Process.* **23** (4), 1103–1114.

Bailey, S.C.C. & Smits, A.J. 2010 Experimental investigation of the structure of large- and very-large-scale motions in turbulent pipe flow. *J. Fluid Mech.* **651**, 339–356.

Balachandar, S. & Eaton, J.K. 2010 Turbulent dispersed multiphase flow. *Annu. Rev. Fluid Mech.* **42** (1), 111–133.

Balakumar, B.J. & Adrian, R.J. 2007 Large- and very-large-scale motions in channel and boundary-layer flows. *Phil. Trans. R. Soc.* A **365** (1852), 665–681.

Baltzer, J.R., Adrian, R.J. & Wu, X. 2013 Structural organization of large and very large scales in turbulent pipe flow simulation. *J. Fluid Mech.* **720**, 236–279.

Banerjee, T., Katul, G.G., Salesky, S.T. & Chamecki, M. 2015 Revisiting the formulations for the longitudinal velocity variance in the unstable atmospheric surface layer. *Q. J. R. Meteorol. Soc.* **141** (690), 1699–1711.

Bourassa, C. & Thomas, F.O. 2009 An experimental investigation of a highly accelerated turbulent boundary layer. *J. Fluid Mech.* **634**, 359–404.

Brandt, L. & Coletti, F. 2022 Particle-laden turbulence: progress and perspectives. *Annu. Rev. Fluid Mech.* **54** (1), 159–189.

Brilouet, P.E., Durand, P., Canut, G. & Fourrié, N. 2020 Organized turbulence in a cold-air outbreak: evaluating a large-eddy simulation with respect to airborne measurements. *Boundary-Layer Meteorol.* **175**, 57–91.

Businger, J.A. & Yaglom, A.M. 1971 Introduction to Obukhov's paper on "turbulence in an atmosphere with a non-uniform temperature". *Boundary-Layer Meteorol.* **2**, 3–6.

Carper, M.A. & Porté-Agel, F. 2004 The role of coherent structures in subfilter-scale dissipation of turbulence measured in the atmospheric surface layer. *J. Turbul.* **5**, N40.

Cassisa, C., Simoens, S., Prinet, V. & Shao, L. 2010 Sub-grid physical optical flow for remote sensing of sandstorm. In *2010 IEEE International Geoscience and Remote Sensing Symposium*, pp. 2230–2233. IEEE.

Chamecki, M., Dias, N.L., Salesky, S.T. & Pan, Y. 2017 Scaling laws for the longitudinal structure function in the atmospheric surface layer. *J. Atmos. Sci.* **74** (4), 1127–1147.

Chauhan, K., Hutchins, N., Marusic, I. & Monty, J. 2010 Two-point correlation statistics in the atmospheric surface layer. In *Proceedings of 17th Australasian Fluid Mech Conference Paper 2010, Auckland, New Zealand*.

Chauhan, K., Hutchins, N., Monty, J. & Marusic, I. 2013 Structure inclination angles in the convective atmospheric surface layer. *Boundary-Layer Meteorol.* **147**, 41–50.

Chen, J. & Xu, Y.L. 2004 On modelling of typhoon-induced nonstationary wind speed for tall buildings. *Struct. Des. Tall Spec. Build.* **13** (2), 145–163.

Cheng, X.L., Zeng, Q.C. & Hu, F. 2011 Characteristics of gusty wind disturbances and turbulent fluctuations in windy atmospheric boundary layer behind cold fronts. *J. Geophys. Res.-Atmos.* **116**, D06101.

Cheynet, E., Jakobsen, J.B. & Obhrai, C. 2017 Spectral characteristics of surface-layer turbulence in the north sea. *Energy Procedia* **137**, 414–427, 14th Deep Sea Offshore Wind R&D Conference, EERA DeepWind 2017.

Chong, K.L., Huang, S.D., Kaczorowski, M. & Xia, K.Q. 2015 Condensation of coherent structures in turbulent flows. *Phys. Rev. Lett.* **115**, 264503.

Christensen, K.T. & Adrian, R.J. 2001 Statistical evidence of hairpin vortex packets in wall turbulence. *J. Fluid Mech.* **431**, 433–443.

Chunchuzov, I.P. 1994 On a possible generation mechanism for nonstationary mountain waves in the atmosphere. *J. Atmos. Sci.* **51** (15), 2196–2206.

Chung, D., Marusic, I., Monty, J.P., Vallikivi, M. & Smits, A.J. 2015 On the universality of inertial energy in the log layer of turbulent boundary layer and pipe flows. *Exp. Fluids* **56**, 141.

COSTANTINI, M., HEIN, S., HENNE, U., KLEIN, C., KOCH, S., SCHOJDA, L., ONDRUS, V. & SCHRÖDER, W. 2016 Pressure gradient and nonadiabatic surface effects on boundary layer transition. *AIAA J.* **54** (11), 3465–3480.

DAI, Y., WILLIAMS, I.N. & QIU, S. 2021 Simulating the effects of surface energy partitioning on convective organization: case study and observations in the US Southern Great Plains. *J. Geophys. Res.-Atmos.* **126**, e2020JD033821.

DAVIDSON, P.A., KROGSTAD, P.A. & NICKELS, T.B. 2006*a* A refined interpretation of the logarithmic structure function law in wall layer turbulence. *Phys. Fluids* **18**, 065112.

DAVIDSON, P.A., NICKELS, T.B. & KROGSTAD, P.A. 2006*b* The logarithmic structure function law in wall-layer turbulence. *J. Fluid Mech.* **550**, 51–60.

DING, M.J., NGUYEN, K.X., LIU, S.S., OTTE, M.J. & TONG, C. 2018 Investigation of the pressure-strain-rate correlation and pressure fluctuations in convective and near neutral atmospheric surface layers. *J. Fluid Mech.* **854**, 88–120.

DJURIC, P.M., KAY, S.M. & BOUDREAUX-BARTELS, G.F. 1992 Segmentation of nonstationary signals. In *IEEE International Conference on Acoustics, Speech, and Signal Processing*, vol. 5, pp. 161–164. IEEE Computer Society.

ELGHOBASHI, S. 1994 On predicting particle-laden turbulent flows. *Appl. Sci. Res.* **52**, 309–329.

EMADZADEH, A., CHIEW, Y.M. & AFZALIMEHR, H. 2010 Effect of accelerating and decelerating flows on incipient motion in sand bed streams. *Adv. Water Resour.* **33** (9), 1094–1104.

EMES, M.J., ARJOMANDI, M., KELSO, R.M. & GHANADI, F. 2019 Turbulence length scales in a low-roughness near-neutral atmospheric surface layer. *J. Turbul.* **20** (9), 545–562.

FALKOVICH, G. 2018 *Fluid Mechanics*, 2nd edn. Cambridge University Press.

FEIGENWINTER, C., VOGT, R. & PARLOW, E. 1999 Vertical structure of selected turbulence characteristics above an urban canopy. *Theor. Appl. Climatol.* **62**, 51–63.

FENTON, L.K., GEISSLER, P.E. & HABERLE, R.M. 2007 Global warming and climate forcing by recent albedo changes on Mars. *Nature* **446**, 646–649.

FERNHOLZ, H.H. & WAENACK, D. 1998 The effects of a favourable pressure gradient and of the Reynolds number on an incompressible axisymmetric turbulent boundary layer. Part 1. the turbulent boundary layer. *J. Fluid Mech.* **359**, 329–356.

FOKEN, T., GOCKEDE, M., MAUDER, M., MAHRT, L., AMIRO, B. & MUNGER, W. 2004 *Post-Field Data Quality Control*, pp. 181–208. Kluwer Academic.

FRENZEN, P. & VOGEL, C.A. 1992 The turbulent kinetic energy budget in the atmospheric surface layer: a review and an experimental reexamination in the field. *Boundary-Layer Meteorol.* **60**, 49–76.

FRISCH, U. & KOLMOGOROV, A.N. 1995 *Turbulence: The Legacy of A.N. Kolmogorov*. Cambridge University Press.

GUALA, M., HOMMEMA, S.E. & ADRIAN, R.J. 2006 Large-scale and very-large-scale motions in turbulent pipe flow. *J. Fluid Mech.* **554**, 521–542.

HASSANPOUR, H., SHAHIRI, M. IEEE, 2007 Adaptive segmentation using wavelet transform. In *2007 International Conference on Electrical Engineering*, pp. 1–5. IEEE.

HEISEL, M., DASARI, T., LIU, Y., HONG, J., COLETTI, F. & GUALA, M. 2018 The spatial structure of the logarithmic region in very-high-Reynolds-number rough wall turbulent boundary layers. *J. Fluid Mech.* **857**, 704–747.

HEISEL, M., SULLIVAN, P.P., KATUL, G.G. & CHAMECKI, M. 2023 Turbulence organization and mean profile shapes in the stably stratified boundary layer: zones of uniform momentum and air temperature. *Boundary-Layer Meteorol.* **186**, 533–565.

HELFER, K.C. & NUIJENS, L. 2021 The morphology of simulated trade-wind convection and cold pools under wind shear. *J. Geophys. Res.-Atmos.* **126**, e2021JD035148.

HÖGSTRÖM, U. 1988 Non-dimensional wind and temperature profiles in the atmospheric surface layer: a re-evaluation. *Boundary-Layer Meteorol.* **42**, 55–78.

HÖGSTRÖM, U., HUNT, J.C. & SMEDMAN, A.S. 2002 Theory and measurements for turbulence spectra and variances in the atmospheric neutral surface layer. *Boundary-Layer Meteorol.* **103**, 101–124.

HOMMEMA, S.E. & ADRIAN, R.J. 2003 Packet structure of surface eddies in the atmospheric boundary layer. *Boundary-Layer Meteorol.* **106**, 147–170.

HUANG, N.E., SHEN, Z., LONG, S.R., WU, M.L.C., SHIH, H.H., ZHENG, Q.N., YEN, N.C., TUNG, C.C. & LIU, H.H. 1998 The empirical mode decomposition and the Hilbert spectrum for nonlinear and nonstationary time series analysis. *Proc. R. Soc.* A **454**, 903–995.

HUANG, S.D., KACZOROWSKI, M., NI, R. & XIA, K.Q. 2013 Confinement-induced heat-transport enhancement in turbulent thermal convection. *Phys. Rev. Lett.* **111**, 104501.

HUNT, J.C.R. & MORRISON, J.F. 2000 Eddy structure in turbulent boundary layers. *Eur. J. Mech. (B/Fluids)* **19** (5), 673–694.

HUTCHINS, N., CHAUHAN, K., MARUSIC, I., MONTY, J. & KLEWICKI, J. 2012 Towards reconciling the large-scale structure of turbulent boundary layers in the atmosphere and laboratory. *Boundary-Layer Meteorol.* **145**, 273–306.

HUTCHINS, N. & MARUSIC, I. 2007 Large-scale influences in near-wall turbulence. *Phil. Trans. R. Soc.* A **365**, 647–64.

ICHIMIYA, M., NAKAMURA, I. & YAMASHITA, S. 1998 Properties of a relaminarizing turbulent boundary layer under a favorable pressure gradient. *Exp. Therm. Fluid Sci.* **17** (1), 37–48.

JEONG, B., BAE, Y.H., LEE, D.S. & KIM, S.W. 1997 Biodegradable block copolymers as injectable drug-delivery systems. *Nature* **388**, 860–862.

JIMÉNEZ, J. 2018 Coherent structures in wall-bounded turbulence. *J. Fluid Mech.* **842**, P1.

JOSHI, P., LIU, X.F. & KATZ, J. 2011 Turbulence in accelerating boundary layers. In *Proceedings of the ASME/JSME/KSME Joint Fluids Engineering Conference 2011, vol. 1, PTS A-D*, pp. 3921–3932. ASME; JSME; KSME.

JUNG, S.Y. & CHUNG, Y.M. 2012 Large-eddy simulation of accelerated turbulent flow in a circular pipe. *Intl J. Heat Fluid Flow* **33** (1), 1–8.

KAIMAL, J.C., WYNGAARD, J.C., IZUMI, Y. & COTÉ, O.R. 1972 Spectral characteristics of surface-layer turbulence. *Q. J. R. Meteorol. Soc.* **98** (417), 563–589.

KAREEM, A., HU, L., GUO, Y.L. & KWON, D.K. 2019 Generalized wind loading chain: time-frequency modeling framework for nonstationary wind effects on structures. *J. Struct. Engng* **145** (10), 04019092.

KATUL, G., KUHN, G., SCHIELDGE, J. & HSIEH, C.I. 1997 The ejection-sweep character of scalar fluxes in the unstable surface layer. *Boundary-Layer Meteorol.* **83**, 1–26.

KATUL, G.G., GHANNAM, K., BOU-ZEID, E., GERKEN, T. & CHAMECKI, M. 2018 Scaling and similarity of the anisotropic coherent eddies in near-surface atmospheric turbulence. *J. Atmos. Sci.* **75** (3), 943–964.

KIM, K.C. & ADRIAN, R.J. 1999 Very large-scale motion in the outer layer. *Phys. Fluids* **11** (2), 417–422.

KIM, S.W. & PARK, S.U. 2003 Coherent structures near the surface in a strongly sheared convective boundary layer generated by large-eddy simulation. *Boundary-Layer Meteorol.* **106**, 35–60.

KLINE, S.J., REYNOLDS, W.C., SCHRAUB, F.A. & RUNSTADLER, P.W. 1967 The structure of turbulent boundary layers. *J. Fluid Mech.* **75**, 741–773.

KOK, J.F. 2010 Difference in the wind speeds required for initiation versus continuation of sand transport on Mars: implications for dunes and dust storms. *Phys. Rev. Lett.* **104**, 074502.

KORALOV, L. & SINAI, Y.G. 2007 *Theory of Probability and Random Processes*, 2nd edn. Springer.

LAVIELLE, M. 1998 Optimal segmentation of random processes. *IEEE Trans. Signal Process.* **46** (5), 1365–1373.

LI, B. & NEUMAN, C.M. 2012 Boundary-layer turbulence characteristics during aeolian saltation. *Geophys. Res. Lett.* **39** (11), L11402.

LI, X.B. & BO, T.L. 2019 An application of quadrant and octant analysis to the atmospheric surface layer. *J. Wind Engng Ind. Aerodyn.* **189**, 1–10.

LI, X.B., HUTCHINS, N., ZHENG, X.J., MARUSIC, I. & BAARS, W. 2022 Scale-dependent inclination angle of turbulent structures in stratified atmospheric surface layers. *J. Fluid Mech.* **942**, A38.

LI, X.L. & ZHANG, H.S. 2012 Seasonal variations in dust concentration and dust emission observed over Horqin Sandy Land area in China from December 2010 to November 2011. *Atmos. Environ.* **61**, 56–65.

LI, R.N., ZHENG, H., O'CONNOR, P., XU, H.S., LI, Y.K., LU, F., ROBINSON, B.E., OUYANG, Z.Y., HAI, Y. & DAILY, G.C. 2021 Time and space catch up with restoration programs that ignore ecosystem service trade-offs. *Sci. Adv.* **7** (14), eabf8650.

LIU, H.Y., BO, T.L. & LIANG, Y.R. 2017 The variation of large-scale structure inclination angles in high Reynolds number atmospheric surface layers. *Phys. Fluids* **29** (3), 035104.

LIU, H.Y., HE, X.B. & ZHENG, X.J. 2023 Amplitude modulation in particle-laden atmospheric surface layers. *J. Fluid Mech.* **957**, A14.

LIU, H.Y., SHI, Y.X. & ZHENG, X.J. 2022 Evolution of turbulent kinetic energy during the entire sandstorm process. *Atmos. Chem. Phys.* **22** (13), 8787–8803.

LIU, H.Y., WANG, G.H. & ZHENG, X.J. 2018 Amplitude modulation between multi-scale turbulent motions in high-Reynolds-number atmospheric surface layers. *J. Fluid Mech.* **861**, 585–607.

LIU, H.Y. & ZHENG, X.J. 2021 Large-scale structures of wall-bounded turbulence in single- and two-phase flows: advancing understanding of the atmospheric surface layer during sandstorms. *Flow* **1**, E5.

LOTFY, E.R., ABBAS, A.A., ZAKI, S.A. & HARUN, Z. 2019 Characteristics of turbulent coherent structures in atmospheric flow under different shear-buoyancy conditions. *Boundary-Layer Meteorol.* **173**, 115–141.

MAHRT, L., NILSSON, E., RUTGERSSON, A. & PETTERSSON, H. 2020 Sea-surface stress driven by small-scale nonstationary winds. *Boundary-Layer Meteorol.* **176**, 13–33.
MARUSIC, I. & MONTY, J.P. 2019 Attached eddy model of wall turbulence. *Annu. Rev. Fluid Mech.* **51** (1), 49–74.
METZGER, M., MCKEON, B.J. & HOLMES, H. 2007 The near-neutral atmospheric surface layer: turbulence and non-stationarity. *Phil. Trans. R. Soc.* A **365**, 859–876.
MONIN, A.S. & OBUKHOV, A.M. 1954 Turbulent mixing in the atmospheric surface layer. *Tr. Inst. Theor. Geofiz* **24**, 163–187.
NAGANO, Y. & TAGAWA, M. 1988 Statistical characteristics of wall turbulence with a passive scalar. *J. Fluid Mech.* **196**, 157–185.
NGUYEN, K.X., HORST, T.W., ONCLEY, S.P. & TONG, C. 2013 Measurements of the budgets of the subgrid-scale stress and temperature flux in a convective atmospheric surface layer. *J. Fluid Mech.* **729**, 388–422.
NILSSON, E., LOHOU, F., LOTHON, M., PARDYJAK, E., MAHRT, L. & DARBIEU, C. 2019 Turbulence kinetic energy budget during the afternoon transition—part 1: observed surface TKE budget and boundary layer description for 10 intensive observation period days. *Atmos. Chem. Phys.* **16** (14), 8849–8872.
OBUKHOV, A.M. 1946 Turbulence in an atmosphere with temperature inhomogeneities. *Tr. Inst. Theor. Geofiz* **1**, 95–115.
PERRY, A.E. & CHONG, M.S. 1982 On the mechanism of wall turbulence. *J. Fluid Mech.* **119**, 173–217.
PIOMELLI, U., BALARAS, E. & PASCARELLI, A. 2000 Turbulent structures in accelerating boundary layers. *J. Turbul.* **1**, N1.
PIOMELLI, U. & YUAN, J.L. 2013 Numerical simulations of spatially developing, accelerating boundary layers. *Phys. Fluids* **25** (10), 101304.
POPE, S.B. 2000 *Turbulent Flows*. Cambridge University Press.
RAO, K.G. & NARASIMHA, R. 2006 Heat-flux scaling for weakly forced turbulent convection in the atmosphere. *J. Fluid Mech.* **547**, 115–135.
RICHARDSON, L.F. 1922 *Weather Prediction by Numerical Process*. Cambridge University Press.
ROBINSON, S.K. 1991 Coherent motions in the turbulent boundary layer. *Annu. Rev. Fluid Mech.* **23** (1), 601–639.
SALESKY, S.T. & ANDERSON, W. 2018 Buoyancy effects on large-scale motions in convective atmospheric boundary layers: implications for modulation of near-wall processes. *J. Fluid Mech.* **856**, 135–168.
SALESKY, S.T., KATUL, G.G. & CHAMECKI, M. 2013 Buoyancy effects on the integral lengthscales and mean velocity profile in atmospheric surface layer flows. *Phys. Fluids* **25** (10), 105101.
SCHULZ, E.W. & SANDERSON, B.G. 2004 Stationarity of turbulence in light winds during the maritime continent thunderstorm experiment. *Boundary-Layer Meteorol.* **111**, 523–541.
SHE, Z.S. & LEVEQUE, E. 1994 Universal scaling laws in fully developed turbulence. *Phys. Rev. Lett.* **72**, 336–339.
DE SILVA, C.M., MARUSIC, I., WOODCOCK, J.D. & MENEVEAU, C. 2015 Scaling of second- and higher-order structure functions in turbulent boundary layers. *J. Fluid Mech.* **769**, 654–686.
SMITS, A.J., MCKEON, B.J. & MARUSIC, I. 2011 High-Reynolds number wall turbulence. *Annu. Rev. Fluid Mech.* **43** (1), 353–375.
SUN, C., XI, H.D. & XIA, K.Q. 2005 Azimuthal symmetry, flow dynamics, and heat transport in turbulent thermal convection in a cylinder with an aspect ratio of 0.5. *Phys. Rev. Lett.* **95**, 074502.
SUN, C., ZHOU, Q. & XIA, K.Q. 2006 Azimuthal symmetry, flow dynamics, and heat transport in turbulent thermal convection in a cylinder with an aspect ratio of 0.5. *Phys. Rev. Lett.* **97**, 074502.
TALAMELLI, A., FORNACIARI, N., WESTIN, J.K.A. & ALFREDSSON, P.H. 2002 Experimental investigation of streaky structures in a relaminarizing boundary layer. *J. Turbul.* **3** (1), N18.
TAMURA, Y., KAWAI, H., UEMATSU, Y., MARUKAWA, H., FUJII, K. & TANIIKE, Y. 1996 Wind load and wind-induced response estimations in the recommendations for loads on buildings, AIJ 1993. *Engng Struct.* **18** (6), 399–411.
THOMAS, D.S.G., KNIGHT, M. & WIGGS, G.F.S. 2005 Remobilization of southern African desert dune systems by twenty-first century global warming. *Nature* **435**, 1218–1221.
TONG, C. & DING, M. 2020 Velocity-defect laws, log law and logarithmic friction law in the convective atmospheric boundary layer. *J. Fluid Mech.* **883**, A36.
TOWNSEND, A.A. 1976 *The Structure of Turbulent Shear Flow*. Cambridge University Press.
TRACY, C.R., WELCH, W.R. & PORTER, W.P. 1980 *Properties of Air: A Manual for Use in Biophysical Ecology*, 3rd edn. The University of Wisconsin.
VOLINO, R.J. 2020 Non-equilibrium development in turbulent boundary layers with changing pressure gradients. *J. Fluid Mech.* **897**, A2.

WALLACE, J.M. 2016 Quadrant analysis in turbulence research: history and evolution. *Annu. Rev. Fluid Mech.* **48** (1), 131–158.

WANG, G.H., GU, H.H. & ZHENG, X.J. 2020 Large scale structures of turbulent flows in the atmospheric surface layer with and without sand. *Phys. Fluids* **32** (10), 106604.

WANG, G.H. & ZHENG, X.J. 2016 Very large scale motions in the atmospheric surface layer: a field investigation. *J. Fluid Mech.* **802**, 464–489.

WANG, H., WU, T., TAO, T.Y., LI, A.Q. & KAREEM, A. 2016 Measurements and analysis of non-stationary wind characteristics at Sutong Bridge in Typhoon Damrey. *J. Wind Engng Ind. Aerodyn.* **151**, 100–106.

WANG, L.P. & STOCK, D.E. 1993 Dispersion of heavy particles by turbulent motion. *J. Atmos. Sci.* **50** (13), 1897–1913.

WANG, S.Q., ZHAO, L., CAO, S.Y., ZHANG, Y.F., YIN, F. & GE, Y.J. 2018 A comparison study on gust factor considering non-stationary effects under typhoon and monsoon conditions. *Adv. Struct. Engng* **21** (12), 1853–1864.

WILCZAK, J.M., ONCLEY, S.P. & STAGE, S.A. 2001 Sonic anemometer tilt correction algorithms. *Boundary-Layer Meteorol.* **99**, 127–150.

WYNGAARD, J.C. 1992 Atmospheric turbulence. *Annu. Rev. Fluid Mech.* **24** (1), 205–233.

WYNGAARD, J.C. & COTÉ, O.R. 1971 The budgets of turbulent kinetic energy and temperature variance in the atmospheric surface layer. *J. Atmos. Sci.* **28** (2), 190–201.

XIE, J.H., DE SILVA, C., BAIDYA, R., YANG, X.I.A. & HU, R. 2021 Third-order structure function in the logarithmic layer of boundary-layer turbulence. *Phys. Rev. Fluids* **6**, 074602.

XIE, Y.C., DING, G.Y. & XIA, K.Q. 2018 Flow topology transition via global bifurcation in thermally driven turbulence. *Phys. Rev. Lett.* **120**, 214501.

XU, C.Q., GUAN, Q.Y., LIN, J.K., LUO, H.P., YANG, L.Q., TAN, Z., WANG, Q.Z., WANG, N. & TIAN, J. 2020 Spatiotemporal variations and driving factors of dust storm events in northern China based on high-temporal-resolution analysis of meteorological data (1960–2007). *Environ. Pollut.* **260**, 114084.

YADAV, A.K., RAMAN, S. & SHARAN, M. 1996 Surface layer turbulence spectra and dissipation rates during low winds in tropics. *Boundary-Layer Meteorol.* **79**, 205–223.

YANG, X.I.A., BAIDYA, R., JOHNSON, P., MARUSIC, I. & MENEVEAU, C. 2017 Structure function tensor scaling in the logarithmic region derived from the attached eddy model of wall-bounded turbulent flows. *Phys. Rev. Fluids* **2**, 064602.

ZHANG, H.S., ZHU, H., PENG, Y., KANG, L., CHEN, J. & PARK, S.U. 2008 Experiment on dust flux during duststorm periods over desert area. *Acta Meteorol. Sin.* **22**, 239–247.

ZHAO, J.H., LONG, X., ZHANG, F., YANG, Y.L., LIU, S.Y. & LIANG, Y. 2020 The role of turbulent coherent structure in sand/dust emissions in a sand/dust storm of the middle China-Mongolia regime. *Chin. J. Geophys.* **63**, 3967–3980.

ZHOU, Q., SUN, C. & XIA, K.Q. 2007 Morphological evolution of thermal plumes in turbulent Rayleigh–Bénard convection. *Phys. Rev. Lett.* **98**, 074501.

ZOU, Z., LI, S., HUANG, J., LI, P., SONG, J., ZHANG, J.A. & WAN, Z. 2020 Atmospheric boundary layer turbulence in the presence of swell: turbulent kinetic energy budget, Monin–Obukhov similarity theory, and inertial dissipation method. *J. Phys. Oceanogr.* **50** (5), 1213–1225.